# Dissecting the functional heterogeneity of glutamatergic synapses with high-throughput optical physiology

Samuel T. Barlow[1,2], Aaron D. Levy[1,2], Minerva Contreras[1,2], Michael C. Anderson[3,#], and Thomas A. Blanpied[1,2,3]

[1]Department of Physiology, University of Maryland School of Medicine, Baltimore, MD 21201, USA.

[2]UM-MIND, University of Maryland School of Medicine, Baltimore, MD 21201, USA.

[3]Program in Neuroscience, University of Maryland School of Medicine, Baltimore, MD 21201, USA.

[#]Current address: Institute for Cell Engineering, Department of Neurology, Johns Hopkins University School of Medicine, Baltimore, MD,

## Abstract

Fluorescent reporters for glutamate release and postsynaptic $Ca^{2+}$ signaling are essential tools for quantifying synapse functional heterogeneity across neurons and circuits. However, leveraging these probes for neuroscience requires scalable experimental frameworks. Here, we devised a high-throughput approach to efficiently collect and analyze hundreds of optical recordings of glutamate release activity at presynaptic boutons in cultured rat hippocampal neurons. Boutons exhibited remarkable functional heterogeneity and could be separated into multiple functional classes based on their iGluSnFR3 responses to single action potentials, paired stimuli, and synaptic parameters derived from mean-variance analysis. Finally, we developed a novel all-optical assay of pre- and postsynaptic glutamatergic synapse function. We deployed iGluSnFR3 with a red-shifted, postsynaptically-targeted $Ca^{2+}$ sensor, enabling direct imaging and analysis of NMDA receptor-mediated synaptic transmission at large numbers of dendritic spines. This work enables direct observation of the flow of information at single synapses and should speed detailed investigations of synaptic functional heterogeneity.

## Introduction

Synapses are the fundamental information processing modules in the brain, performing computations that dictate how electrical activity propagates across neural circuits[1,2]. Thus, a major goal for neuroscience is to identify the basic functional properties of individual synapses which define their computational output, such as vesicle release probability ($P_r$)[3], the magnitude and variance of receptor activation, and short-term plasticity behavior[4]. However, the enormous diversity that exists among synapses is a significant barrier to achieving a quantitative understanding of synaptic function. The distinct transcriptomic identities of pre- and postsynaptic neurons drive expansive proteomic diversity among synapses[5], and synapses are also plastic, with further speciation emanating from each synapse's unique history of activity[6]. Synapse functional diversity is reflective of this deep proteomic diversity, with $P_r$ varying widely between synapse types (0.05 to 1)[3]. $P_r$ can fluctuate across stimulus frequencies as new vesicle populations[7] or short-term plasticity mechanisms are engaged[4], properties which also exhibit a dependence on synapse identity[7,8]. How these permutations of presynaptic properties impact the activation probability of NMDA receptors (NMDARs) will define which patterns of activity lead to synapse strengthening or weakening[9], constituting another axis of synaptic heterogeneity with implications for neural circuit development.

Due to their expansive diversity, a quantitative understanding of synaptic communication across single neurons and circuits will only be achieved through a synapse-by-synapse readout of synaptic function. Optical methods are well-positioned to meet this need, and direct measurement of synaptic functional properties has been demonstrated using a variety of fluorescent indicators[10,11,12,13,14]. However, several barriers must be overcome to leverage these tools at scale. First, detailed dissection of synaptic function requires a variety of stimulation protocols, chemical conditions, and imaging modalities, resulting in complex experimental paradigms. To acquire these data efficiently and reproducibly, it is desirable to fully automate microscopy, electrical stimulators, and fluidics. Second, to process large datasets, automated segmentation methods that can extract and analyze the same synapses across hundreds of video recordings are essential. Third, intensity-time recordings from individual synapses must be baseline-corrected and normalized to ΔF/F before fluorescence signals can be extracted and analyzed. Indeed, major software packages have been developed to accelerate segmentation and fluorescence signal extraction for calcium (e.g. CaImAn[15], FIOLA[16]) and voltage imaging (e.g. VolPy[17]) *in vivo*, but there are no comprehensive software packages for analysis of synaptic function. Finally, fluorescence data must be converted to interpretable statistics for insight into synaptic functional properties.

Here, we set out to develop all-optical methods to measure the functional heterogeneity of single synapses in cultured rat hippocampal neurons. We focused on the third-generation intensity-based glutamate sensing fluorescent reporter (iGluSnFR3)[18], which allows robust detection of glutamate release from single presynapses to provide quantitative access to basic functional properties such as basal release probability[19] and short-term plasticity dynamics[20]. Existing software packages[15,16,17] possess solutions for drift correction, segmentation, and intensity-time trace analysis, but none were specialized for analysis of iGluSnFR3 recordings, and large segments of the code base were either unnecessary or challenging to customize. We therefore developed a modular approach, enabling end-to-end, high-throughput collection and analysis of hundreds of iGluSnFR3 recordings, through a combination of hardware automation, batch segmentation, and automatic analysis of iGluSnFR3 fluorescence transients. Our scalable, versatile approach enabled deep functional profiling of presynaptic functional heterogeneity (e.g. number of quanta released, $P_r$, paired-pulse ratio) across hundreds of boutons, which enabled us to separate boutons into functional classes according to their iGluSnFR3 responses. Finally, we extended our approach across the synaptic cleft by combining iGluSnFR3 with a red-shifted, postsynaptically-targeted $Ca^{2+}$ reporter to simultaneously image the ionotropic activation of postsynaptic NMDARs by endogenous glutamate release at single dendritic spines. Directly imaging the flow of information during synaptic transmission at single dendritic spines will enable detailed interrogation of synaptic functional heterogeneity and the patterns of glutamatergic activity which favor NMDAR-mediated plasticity induction. These innovations lay the groundwork for synapse-by-synapse structure-function analyses to untangle synapse heterogeneity across single neurons and circuits.

## Results

*A high-throughput framework for analyzing glutamate release from single boutons with iGluSnFR3*

We sought to leverage iGluSnFR3[18] to characterize the heterogeneous glutamate release properties of individual presynaptic boutons in cultured rat hippocampal neurons. To accelerate experimental throughput and improve reproducibility, we devised an automated framework for efficiently collecting large datasets (**Figure 1**). We used microscopy software from Andor (Fusion) and their *Python*-accessible REST API to communicate with our microscope (**Figure 1A**). With the REST API, we wrote imaging protocols that captured stimulus-evoked or spontaneous iGluSnFR3 activity with widefield imaging along axonal arbors at 200 Hz, followed by high-resolution, confocal z-stacks for an arbitrary number of imaging positions. Custom *Python* scripts allowed flexible, fully automated control of both electrical stimulation and solution exchange, enabling the design of versatile experiments to probe the physiological properties of presynaptic boutons using iGluSnFR3.

To capture iGluSnFR3 activity localized to presynaptic boutons, we transfected hippocampal neurons with iGluSnFR3 and Synaptophysin-mRuby, a fluorescent marker which labels the synaptic vesicle (SV) pool at boutons[21]. We used a custom ImageJ macro based on the AI-based ImageJ plugin SynQuant[22] to batch segment Synaptophysin-mRuby puncta within the boundary of iGluSnFR3⁺ axonal arbors. We applied these maps of regions-of-interest (ROIs) to our iGluSnFR3 timelapses (**Figure 1B**), tracking single boutons across many imaging rounds. Alternatively, we could batch segment videos using iGluSnFR3 activity itself by modifying a *MATLAB* script developed previously by Mendonça and colleagues[23] (**Figure 1C**). Activity-based segmentation was useful for expediting analysis (our implementation did not rely on pre-processing steps, e.g. drift correction) or in situations where a synapse marker could not be co-expressed. However, activity-based segmentation also fails to capture inactive synapses, biasing subsequent statistical measures of presynaptic function. Despite its requirement for more image processing, we chose to use a fluorescent marker to track synapses where possible.

We frequently identified 20 or more ROIs along axonal arbors in single imaging regions (25.6 x 25.6 µm). In some experiments, we recorded the same imaging region more than 40 times, resulting in >800 intensity-time traces of iGluSnFR3 activity to be analyzed per region. With multiple regions in a single experiment, we required a scalable solution for extracting relevant iGluSnFR3 activity for analysis. We developed a custom algorithm in *R* based on a median filter, which automatically corrects baseline fluctuations due to noise and identifies iGluSnFR3 signals caused by stimulus-evoked and spontaneous glutamate release at single boutons (**Figure 1D**). Briefly, a rolling median filter was used to approximate the baseline and identify intensity outliers. Outlier detection was refined in subsequent steps to estimate where putative iGluSnFR3 transients occurred, and these were excluded from a smoothed estimate of the baseline. From the baseline-corrected trace, we extracted

103 iGluSnFR3 transients for downstream analysis using a signal threshold of 5σ, where σ is the standard deviation
104 of the noise. **Figure 1E** shows an exemplar stimulus-evoked iGluSnFR3 transient and the intrinsic peak
105 parameters we analyzed: peak amplitude (peak ΔF/F), fitted exponential decay time constant ($\tau_{decay}$), the full-
106 width at half-maximum ($t_{1/2}$), 10-90% rise time ($t_{rise}$), 90-10% decay time ($t_{decay}$), and the time-to-peak following
107 electrical stimulation (Δ$t$).

*Batch segmentation methods extract quantal, spontaneous iGluSnFR3 activity localized to boutons*

110 Action potential (AP)-independent, spontaneous glutamate release events should localize to putative
111 presynaptic boutons marked by Synatophysin-mRuby. To test whether our automated approach could capture
112 this, we imaged spontaneous iGluSnFR3 activity at axonal arbors co-expressing iGluSnFR3 and Synaptophysin-
113 mRuby in a modified Tyrode's buffer containing 1 μM tetrodotoxin (TTX) and either 0.5, 1, 2, or 4 mM $Ca^{2+}$
114 ($[Ca^{2+}]_{bath}$), segmenting recordings according to Synaptophysin-mRuby expression or iGluSnFR3 activity. **Figure**
115 **2A** shows an exemplar imaging region with many putative boutons. **Figure 2B** shows the boutons (blue)
116 collected by our fluorescent marker segmentation compared to activity-based segmentation (red) for a single
117 imaging trial. Notably, while activity segmentation appears to merge the responses of multiple boutons in some
118 instances, the strong concordance of activity ROIs with boutons expressing Synaptophysin-mRuby suggests
119 that both methods can capture iGluSnFR3 activity localized to single boutons. **Figure 2C** shows the average
120 number of ROIs collected per video with each method; the lower number of ROIs collected by activity
121 segmentation reflects that not every bouton will spontaneously release glutamate during the imaging period (30
122 s). However, we also note that our implementation of activity segmentation relies on thresholding activity maps
123 on the top 3% of all pixel intensities. Boutons with low signal-to-noise ratio (SNR) can escape detection (**Figure**
124 **1C**), which may underestimate the number of active boutons.

125 The average iGluSnFR3 response collected by our high-throughput approach showed little variation in
126 iGluSnFR3 transient shape across $[Ca^{2+}]_{bath}$ when compared within segmentation method (**Figure 2D**), reflecting
127 that spontaneous iGluSnFR3 transients are attributable to glutamate release from single SVs at all $[Ca^{2+}]_{bath}$.
128 Activity-based segmentation always resulted in a larger average iGluSnFR3 response, likely because activity
129 segmentation captures the site of maximal iGluSnFR3 signal, i.e. the putative SV release site. By contrast,
130 marker-based segmentation may be subject to orientation effects that reduce SNR, such that the maximal
131 iGluSnFR3 signal could be offset from the SV cloud marked by Synaptophysin-mRuby (visible in top-right, **Figure**
132 **2B**). **Figure 2E-G** show the normalized histograms for selected iGluSnFR3 event parameters across $[Ca^{2+}]_{bath}$
133 and segmentation method. None of the distributions of peak parameters varied substantially in magnitude across
134 $[Ca^{2+}]_{bath}$ when compared within segmentation method. Comparing our segmentation approaches, activity
135 segmentation produced iGluSnFR3 events with larger amplitudes and smaller $\tau_{decay}$, supporting the conclusion
136 that activity segmentation produces ROIs more likely to capture true glutamate release hotspots. However, our
137 data also indicate that Synaptophysin-mRuby segmentation reliably captures quantal activity at putative single
138 boutons. For our subsequent experiments, we used Synaptophysin-mRuby segmentation, which enabled us to
139 track bouton behavior even when boutons were inactive.

*Estimating the number of synaptic vesicles released during evoked transmission*

142 The number of SVs released following an AP is a critical determinant of the strength of transmission[24].
143 This can be assessed at single synapses using SV-targeted pHluorins to directly count released SVs[13] and
144 measure the $P_r$ of SV release sites at single boutons following an AP[25,26]. Conversely, the total number of fusion-
145 competent SVs available to be released during an AP, called the readily releasable pool (RRP)[27], can be
146 measured using mean-variance analysis (MVA)[28]. MVA is typically applied to electrophysiology recordings to
147 calculate the size of the RRP through the relationship $I = N_{sites} \times P_r \times Q$, where $I$ is the mean amplitude of the
148 postsynaptic receptor current, $N_{sites}$ is the total number of release sites in the RRP, $P_r$ is the uniform release
149 probability for the SVs in the RRP, and $Q$ is the current associated with a single SV. However, electrophysiology
150 generally measures presynaptic properties of ensembles of synapses, whereas single-synapse resolution
151 requires fortuitous circuit architecture[29,30]. Optical sensors which directly monitor glutamate release (e.g.
152 iGluSnFR3) go beyond pHluorin imaging or electrophysiology, accessing both the relative magnitude of
153 glutamate release during a single AP and the total size of the RRP through MVA[31] with single-synapse resolution.

Since iGluSnFR3 is sensitive to putative single SV release events, we reasoned that our high throughput approach should be able to determine both how many SVs are released per AP and the overall size of the RRP, enabling determination of the RRP fraction mobilized during each AP at single bouton resolution. To achieve this, we imaged the iGluSnFR3 response evoked by a single AP (10 trials, 20 s between trials) at boutons labeled by Synaptophysin-mRuby ($n$=244 boutons) across different $[Ca^{2+}]_{bath}$ (0.5, 1, 2, and 4 mM). **Figure 3A** compares the average evoked iGluSnFR3 response at each $[Ca^{2+}]_{bath}$ to the average spontaneous response (spontaneous data corresponds to marker-based segmentation data from **Figure 2**). The amplitude of evoked iGluSnFR3 transients increased substantially with increasing $[Ca^{2+}]_{bath}$ as more SVs were released during each AP, in contrast to spontaneous iGluSnFR3 transients, which did not increase in amplitude (**Figure 3B**). From the normalized histograms of peak $\Delta F/F$ and $\tau_{decay}$, (**Figure 3C-D**), we observed that the statistics for evoked iGluSnFR3 events at $[Ca^{2+}]_{bath}$ = 0.5 mM exhibited substantial overlap with their spontaneous counterparts, suggesting boutons only release a single SV per AP at this $[Ca^{2+}]_{bath}$. Most boutons transitioned to releasing multiple SVs per stimulus as $[Ca^{2+}]_{bath}$ increased (**Figure 3C**).

To count the SVs released per AP, we normalized the peak $\Delta F/F$ of each evoked iGluSnFR3 response ($E_{\Delta F/F}$) to the population average of the spontaneous iGluSnFR3 responses ($S_{\Delta F/F}$). **Figure 3E** shows the average value of $E_{\Delta F/F}/S_{\Delta F/F}$ vs. $[Ca^{2+}]_{bath}$, where each colored point is the average response of a single bouton. At 0.5 mM $Ca^{2+}$, the few boutons that were active released approximately 1 SV ($E_{\Delta F/F}/S_{\Delta F/F}$ = 1.12 ± 0.01), while at 4 mM $Ca^{2+}$, boutons released approximately 8.5 vesicles per AP ($E_{\Delta F/F}/S_{\Delta F/F}$ = 8.48 ± 0.32). Ultrastructural observations of boutons in cultured mouse hippocampal neurons indicate that there are 10.1 ± 4.3 (mean ± s.d.) docked SVs per active zone[32], suggesting that at 4 mM $Ca^{2+}$, most boutons in our sample release >80% of the SVs in the RRP. However, some boutons released > 20 putative SVs per AP at 4 mM $Ca^{2+}$, implying that a subset of boutons in our sample either experienced synaptic crosstalk or possessed multiple active zones.

To better understand what fraction of the RRP was mobilized per AP at individual boutons, we fit the mean ($\bar{x}$) and variance ($\sigma^2$) of the $E_{\Delta F/F}/S_{\Delta F/F}$ values for each bouton with a uniform probability binomial model[28], $\sigma^2 = Q\bar{x} - \bar{x}^2/N_{sites}$ (**Figure 3F**). Of the 244 boutons in our sample, 122 possessed mean-variance behavior that was well described by the model, yielding an average RRP size of $N_{sites}$ = 9.05 ± 0.63 (**Figure 3G**), in good agreement with previous ultrastructural measurements and within the range of $N_{sites}$ (1-10) observed by other glutamate imaging methods[19,31]. Of these 122 boutons, most were quiescent at 0.5 mM $Ca^{2+}$ ($E_{\Delta F/F}/S_{\Delta F/F}$ = 0.101 ± 0.013), but at 1, 2, and 4 mM $Ca^{2+}$ boutons released 1.11 ± 0.08, 3.89 ± 0.22, and 4.98 ± 0.25 SVs, respectively. When we compared estimated SV release (i.e. mean $E_{\Delta F/F}/S_{\Delta F/F}$) to RRP size at each bouton, we found that at 1, 2, and 4 mM $Ca^{2+}$, boutons mobilized 13.7%, 50.4%, and 63.8% of their total RRP, respectively (**Figure 3H**). Taken together, our method extends previous approaches by directly comparing the RRP size calculated from MVA with the approximate number of SVs released per AP at single boutons, permitting a direct assessment of presynaptic efficacy. This approach could provide further access to the time constants associated with vesicle recycling and release site replenishment at individual boutons by measuring how the fraction of RRP released per AP changes with stimulus frequency[27].

*Tracking the glutamate release behavior of single boutons reveals three classes of boutons*

The high information content of our iGluSnFR3 recordings suggested that boutons could be classified according to their stimulated iGluSnFR3 response behavior. We examined a set of bouton features for each of the 244 boutons in our sample to characterize their iGluSnFR3 behavior in response to a single AP. First, we calculated the probability of observing stimulus-evoked iGluSnFR3 activity ($P_{iGlu}$) for each bouton across $[Ca^{2+}]_{bath}$ (**Figure 4A**). At $[Ca^{2+}]_{bath}$ = 0.5 mM, most boutons were quiescent ($P_{iGlu}$ = 0.16 ± 0.01), but $P_{iGlu}$ increased sharply at $[Ca^{2+}]_{bath}$ = 1 mM ($P_{iGlu}$ = 0.68 ± 0.02). At $[Ca^{2+}]_{bath}$ = 4 mM, almost all boutons exhibited iGluSnFR3 activity ($P_{iGlu}$ = 0.96 ± 0.01), suggesting nearly all boutons in our sample were glutamatergic or near enough to a glutamatergic synapse to experience glutamate spillover during periods of strong glutamate release. We also calculated the coefficient of variation (CV) across trials for intrinsic peak parameters, including peak $\Delta F/F$ (**Figure 4B**), $\tau_{decay}$ (**Figure 4C**), and $\Delta t$ (**Figure 4D**). For $\Delta t$ and $\tau_{decay}$, the interquartile range (IQR) of the CV distributions decreased as $[Ca^{2+}]_{bath}$ increased (**Fig. 4C-D**), indicating that the onset and decay kinetics of evoked iGluSnFR3 responses between trials became more uniform with increasing $Ca^{2+}$ availability for each bouton. The trend for CV of peak $\Delta F/F$ ($CV_{\Delta F/F}$) was more complex. At 0.5 mM $Ca^{2+}$, the few boutons that were

205 active could only release a single SV following stimulation (**Figure 3F**), biasing $CV_{\Delta F/F}$ toward small values. By
206 contrast, at all other $[Ca^{2+}]_{bath}$ we observed a broad range of $CV_{\Delta F/F}$ values, suggesting the number of SVs
207 released at individual boutons varied between stimuli.

208 Adding these statistics together with the mean amplitude and variance of the iGluSnFR3 response at
209 each $[Ca^{2+}]_{bath}$, we thus compiled 24 features for each bouton that could be analyzed for their relationship to one
210 another using uniform manifold approximation and projection (UMAP)[33]. **Figure 4E** shows the UMAP
211 representation of the 244 boutons, which clustered into three different classes of boutons. **Figure 4F** shows the
212 trends in $P_{iGlu}$ according to cluster identity (cluster ID), revealing that Class 1 boutons were almost always active
213 at $[Ca^{2+}]_{bath}$ = 1 mM ($P_{iGlu}$ = 0.89 ± 0.02), while Class 3 boutons were only active once every 5 stimuli ($P_{iGlu}$ = 0.19
214 ± 0.03). When SVs were in their lowest $P_r$ state at 0.5 mM $Ca^{2+}$, active Class 1 boutons reliably released a single
215 SV ($E_{\Delta F/F}/S_{\Delta F/F}$ = 1.16 ± 0.04) while Class 2 and 3 boutons were categorically quiescent (**Figure 4G**). When SVs
216 were in their highest $P_r$ state at 4 mM $Ca^{2+}$, Class 1 boutons released ~10 SVs, >3-fold more than Class 3
217 boutons (Class 1: $E_{\Delta F/F}/S_{\Delta F/F}$ = 10.3 ± 0.5, Class 3: $E_{\Delta F/F}/S_{\Delta F/F}$ = 3.1 ± 0.2). Thus, large-scale functional analysis
218 is suitable to classify synapses based purely on presynaptic release characteristics, highlighting the utility of the
219 imaging and analysis pipeline. Future efforts could easily incorporate other non-functional characteristics into
220 UMAP classification, e.g. intensity of the fluorescent presynaptic marker or region size.

221 To examine the basis of the observed functional classification, we mapped the cluster IDs onto the bouton
222 parameters extracted from MVA. The distribution of $N_{sites}$ according to cluster ID suggested that the fidelity and
223 magnitude with which Class 1 boutons responded to stimuli could be explained by their larger RRPs (Class 1:
224 $N_{sites}$ = 14.7 ± 2.0, **Figure 4H**). These large RRPs imply Class 1 boutons possess multiple active zones, but we
225 also note these boutons possessed faster iGluSnFR3 kinetics (smaller $\Delta t$, $t_{rise}$, $\tau_{decay}$) with lower variance in their
226 response on all metrics relative to Class 2 and 3 boutons (**Extended Data Figure 4**). Interestingly, the calculated
227 $P_r$ of SV release sites was very similar for all boutons in the dataset regardless of cluster ID. We speculate that
228 while release site organization relative to $Ca^{2+}$ channel clusters and/or $Ca^{2+}$ influx during the AP may be similar
229 across bouton classes, the release sites at Class 1 boutons are more functionally mature, driving SV fusion in a
230 faster and more synchronized fashion following an AP.

231 A key advantage of optical physiology is that functional heterogeneity is spatially resolved. To visualize
232 how bouton physiology varies along the axonal arbor, we mapped cluster IDs to their originating axonal arbors
233 (**Figure 4I**). To aid visual comparison across boutons, the script generates a "Bouton Report" for each bouton
234 that summarizes key features. **Figure 4J-M** shows an example Bouton Report for Bouton 34, which includes the
235 iGluSnFR3 response for all 40 single-stimulus trials (**Figure 4J**), a comparison of $P_{iGlu}$ with the observed uniform
236 $P_r$ from MVA (**Figure 4K**), the estimated SVs released per AP for each trial (**Figure 4L**), and the binomial fit of
237 the mean-variance curve (**Figure 4M**). Together, these tools enable scalable, functional profiling of individual
238 boutons with high information content, and will aid development of single synapse "function-omics".

239

240 *Paired stimuli reveal heterogeneous short-term plasticity across single boutons*

241 The presynaptic terminal can contribute to synapse computation via short-term plasticity, in which pairs
242 of stimuli delivered in short succession can drive increased (facilitation) or decreased (depression)
243 neurotransmitter release on the second pulse[4]. Encouraged by the heterogeneity we observed in our single
244 stimulus experiments, we next asked whether our high-throughput approach could capture similar diversity in
245 the short-term plasticity at single boutons. We imaged axonal arbors co-expressing iGluSnFR3 and
246 Synaptophysin-mRuby, and recorded iGluSnFR3 activity in response to a battery of stimulus paradigms,
247 including a single stimulus (test pulse) and paired stimuli separated by inter-stimulus intervals (ISIs) of 60, 75,
248 100, 150, or 500 ms. For each region, each of these stimulus protocols was administered in triplicate (20 s
249 between trials). We began each imaging session with $[Ca^{2+}]_{bath}$ = 0.5 mM, administering the protocol sequence
250 before washing in buffer containing 1 mM or 2 mM $Ca^{2+}$. We collected iGluSnFR3 activity from 149 putative
251 boutons at 6 neurons. At $[Ca^{2+}]_{bath}$ = 0.5 mM, more than 75% of boutons failed to respond at all ISIs, so we
252 present our analysis below with only $[Ca^{2+}]_{bath}$ = 1 and 2 mM.

253 **Figure 5A** shows the averaged iGluSnFR3 responses for each protocol and $[Ca^{2+}]_{bath}$. Our goal was to
254 directly measure the paired-pulse ratio (PPR) at single boutons, capturing heterogeneous short-term plasticity
255 behavior along the axonal arbor – however, the kinetics of iGluSnFR3 result in a convolution of the responses

256 to the 1st and 2nd stimuli at ISIs ≤ 150 ms, obscuring the true amplitude of the 2nd stimulus response. To
257 circumvent this, we subtracted the average response to a single stimulus at each bouton from the responses for
258 each paired pulse trial, allowing measurement of the 2nd stimulus response at all ISIs (**Figure 5B**), and
259 subsequently, PPRs for each bouton for each stimulus protocol. **Figure 5C** shows the measured PPRs at all
260 ISIs and $[Ca^{2+}]_{bath}$. At $[Ca^{2+}]_{bath}$ = 2 mM, most boutons depressed, consistent with an elevated initial release
261 probability that depletes release sites following the 1st stimulus and failure to dock and prime new SVs prior to
262 the 2nd stimulus. By contrast, at $[Ca^{2+}]_{bath}$ = 1 mM we observed that boutons could facilitate, depress, or exhibit
263 no change in their response at the second stimulus for all ISIs. To ask whether boutons exhibited heterogeneous
264 short-term plasticity dynamics, we measured which ISI generated the largest PPR at each bouton. We observed
265 that 49% of boutons exhibited a "facilitation preference" for our shortest measured ISI at 60 ms (**Figure 5D**).
266 Intriguingly, the facilitation preference for the second largest category of boutons (18%) was at ISI = 100 ms,
267 suggesting boutons possess diverse time constants which describe their short-term plasticity dynamics.

268     To better understand the heterogeneity of facilitation behavior across the axonal arbor, we mapped the
269 facilitation preference (**Figure 5E**) and PPRs for selected ISIs (60, 100 ms, **Figure 5F,G**) at $[Ca^{2+}]_{bath}$ = 1 mM for
270 an exemplar imaging region. Boutons in this imaging region were liable to preferentially facilitate at any of the
271 ISIs tested except for 500 ms. We selected two boutons with divergent properties for targeted analysis, Bouton
272 5 (upper left, **Figure 5E**, analysis **Figure 5H, I**) and Bouton 9 (middle right, **Figure 5E**, analysis **Figure 5J, K**).
273 Strikingly, while Bouton 5 and 9 possessed similar glutamate release magnitudes (**Figure 5H, J**), they diverge
274 strongly in the presentation of their PPR curves (**Figure 5I, K**), suggesting that while they may operate using
275 similar numbers of release sites, distinctive mechanisms mediate their facilitation behavior. The functional
276 imaging toolkit demonstrated here could be combined with post-hoc immunocytochemistry or super-resolution
277 imaging of synaptic proteins to define how protein expression and organization at the synapse drive diverse
278 short-term plasticity behavior across single neurons.

279

280 *Simultaneous imaging of iGluSnFR3 and a far-red $Ca^{2+}$ reporter enables direct, all-optical*
281 *measurement of NMDAR-mediated synaptic transmission at single dendritic spines*

282     In standard postsynaptic patch-clamp recordings, measures of presynaptic function are indirect and
283 postsynaptic measures lack spatial specificity. Dual optical assays of pre- and postsynaptic function will be
284 required to untangle the basic functional properties of single synapses. To address this need, we focused on
285 detecting activation of NMDARs, since dysregulated NMDAR-mediated synaptic transmission is implicated in
286 plasticity and multiple neuropsychiatric illnesses[34]. We paired iGluSnFR3 with a red-shifted $Ca^{2+}$ reporter
287 targeted to the dendritic spine to allow us to directly resolve NMDAR-mediated synaptic transmission at individual
288 dendritic spines with simultaneous presynaptic readout. Previous work introduced spine-jRGECO1a[35], a fusion
289 construct that expresses jRGECO1a in actin-rich compartments of the cell like the dendritic spine. However, 488
290 nm light causes jRGECO1a to photoswitch[36], dramatically reducing SNR and rendering spine-jRGECO1a
291 incompatible with iGluSnFR3 in our hands. To avoid this, we replaced the coding sequence for jRGECO1a with
292 that of HaloTag[37], which could we labeled with a far-red chemigenetic $Ca^{2+}$ sensor, $JF_{646}$-BAPTA-
293 HaloTagLigand-AM[38] (hereafter, $JF_{646}$-BAPTA). Co-expression of iGluSnFR3 with spine-HaloTag thus enabled
294 simultaneous access to dendritic spine glutamate and $Ca^{2+}$ dynamics (**Figure 6A, B**).

295     To observe NMDAR activation by spontaneously released glutamate, we imaged hippocampal neurons
296 co-expressing iGluSnFR3 and spine-HaloTag in buffer with 4 mM $Ca^{2+}$, 0 mM $Mg^{2+}$, and 1 μM TTX[39]. We
297 segmented these recordings by iGluSnFR3 activity, observing iGluSnFR3 transients localized to dendritic spines
298 that were often (but not always) followed by a $JF_{646}$-BAPTA transient (**Figure 6B**). To analyze these, we used
299 the iGluSnFR3 peaks detected by our algorithm to guide our identification of correlated $JF_{646}$-BAPTA peaks. We
300 considered these event pairs to be putative synaptic transmission events if the $JF_{646}$-BAPTA amplitude exceeded
301 a threshold of +3.5σ (σ is the standard deviation of the $JF_{646}$-BAPTA baseline, **Figure 6B, C**).

302     To determine whether these $JF_{646}$-BAPTA signals represent NMDAR activation by glutamate, we imaged
303 neurons before and after perfusion of an NMDAR antagonist, AP5, or a control solution. For most spines, the
304 amplitude correlation between iGluSnFR3 and $JF_{646}$-BAPTA signals remained the same following perfusion of
305 control solution, but perfusion of 100 μM AP5 abolished $JF_{646}$-BAPTA signals without affecting iGluSnFR3
306 (**Extended Data Figure 6**). When we time-aligned transmission events and averaged them together (**Figure**

**6D**), it became obvious that AP5 treatment abolished $JF_{646}$-BAPTA events, indicating that this $Ca^{2+}$ activity originated from NMDAR activation. By contrast, the amplitude of iGluSnFR3 events after wash-in of either solution decreased similarly, presumably due to photobleaching.

The high steady-state affinity of NMDARs has often been taken to indicate that even the glutamate released from single vesicles will be sufficient to maximize activation of all NMDARs in a synapse. On the contrary, we observed many spines which exhibited a dose-dependent behavior similar to **Figure 6B,C**, suggesting large glutamate transients activate greater numbers of NMDARs. To analyze this, we normalized for spine-to-spine variation in iGluSnFR3 and $JF_{646}$-BAPTA by converting each spine's distribution of amplitudes to z-scores (**Figure 6E**). Similar to the single spine behavior of **Figure 6B,C**, at the population level we observed a strong positive correlation between $JF_{646}$-BAPTA and iGluSnFR3 amplitudes before and after perfusion with a control solution. By contrast, treatment with AP5 abolished the amplitude correlation. Remarkably, rare spines exhibited $Ca^{2+}$ responses following large iGluSnFR3 transients even after AP5 treatment (**Figure S1**). Such rare events would typically not be detected by electrophysiology and indeed may not be associated with current flux. They may indicate that glutamate can transiently out-compete AP5 to trigger NMDAR-mediated $Ca^{2+}$ flux when the glutamate concentration in the synaptic cleft is sufficiently large[40]. Alternatively, it could reveal the presence in such synapses of other glutamate-triggered intracellular $Ca^{2+}$ signaling, most likely through metabotropic glutamate receptors[41]. By accessing both pre- and postsynaptic function during NMDAR-mediated synaptic transmission *in situ* at single dendritic spines, we anticipate our approach will both enable new lines of inquiry into the biophysics of NMDAR activation during complex activity patterns, and further be suitable for examining control of diverse signaling events during synaptic transmission.

Finally, we mapped the number of transmission events ($N_{transmission}$) at an exemplar imaging region to appraise the heterogeneous activity across the dendritic arbor (**Figure 6F**). $N_{transmission}$ for this imaging region varied from 1 event to >10 events over the 30 s imaging epoch. We selected two spines with similar activity profiles for further analysis, comparing their collected transmission events in **Figure 6G,H**. To our surprise, we observed distinct decay kinetics for $JF_{646}$-BAPTA events between Spine 4 and Spine 20, while the overall magnitude of $JF_{646}$-BAPTA transients were similar (**Figure 6I**). The observation of kinetic differences between spines would be consistent with distinct expression of NMDAR subtypes. We expect that these single spine recordings could be paired with super-resolution imaging of synaptic NMDARs. Such an approach could resolve open questions about how synaptic function is modified by the observed preference of NMDARs for certain glutamate release sites.

## Discussion

Here, we developed a high-throughput optical physiology approach to address several aspects of synaptic functional heterogeneity in hippocampal neuron cultures. First, leveraging high-speed and high-content analysis of iGluSnFR3 responses across large numbers of boutons, we observed broad diversity in synaptic transmission strength across boutons, as both the estimated number of SVs released per stimulus and RRP size exhibited broad inter-bouton variation. Second, by enabling systematic analysis of responses probed with complex stimulus paradigms and across multiple ionic or pharmacological conditions, we provide a path to identification and deep characterization of synaptic functional classes. Indeed, we observed diverse short-term plasticity behavior and found that even boutons near one another and with similar basal release properties could exhibit a large range of paired-pulse facilitation dynamics. Last, we leveraged our high-throughput approach to measure pre- and postsynaptic functional properties simultaneously, accessing NMDAR-mediated synaptic transmission at single spines by pairing iGluSnFR3 with a red-shifted $Ca^{2+}$ sensor ($JF_{646}$-BAPTA). This approach enables future investigations to determine the patterns of glutamatergic activity which favor NMDAR activation across synapse types and how these may be disrupted in disease models which feature NMDAR dysfunction. We expect that our high-throughput optical physiology approach opens new lines of inquiry into synaptic functional heterogeneity across single neurons and circuits.

Our approach combined three key technical innovations. First, we devised an automated hardware scheme controlled entirely by a *Python* script that supports the design of complex, versatile experiments which featured multiple imaging modes, stage locations, stimulus protocols, and fluid exchange rounds. Second, we developed a suite of easily customized scripts across *ImageJ* and *MatLab* for batch drift correction and

segmentation of optical physiology recordings. *R*-based file handling routines automatically matched recordings of synaptic activity to their appropriate maps of ROIs, allowing facile tracking the iGluSnFR3 activity at boutons across 40+ imaging rounds. Third, our custom *R* algorithm automatically corrected the baseline and normalized intensity-time traces, enabling the analysis of 10,000+ traces in tens of minutes on standard computers and automating the production of customizable outputs ranging from single-synapse functional reports to fully publication-quality summary figures. Further, the algorithm extracted iGluSnFR3 transients according to the published kinetics of the fluorescent biosensor being imaged – in principle, our algorithm can perform baseline correction, trace normalization, and feature extraction for a variety of fluorescent biosensors (including GCaMPs and voltage sensors). Together, these innovations constituted a data collection and analysis framework which shortened the time lag between experiments and publication-quality figures from weeks to days.

A fundamental parameter underlying synaptic strength is the number of SVs mobilized per AP, and understanding how this property varies across neurons and circuits is crucial to understanding how information flows in the brain. We used our high-throughput approach to directly estimate how many SVs were released per stimulus at fields of single boutons by using quantal, AP-independent iGluSnFR3 transients as the benchmark for glutamate release from a single SV ($E_{\Delta F/F}/S_{\Delta F/F}$). As $P_r$ increased, boutons exhibited broad diversity in SVs released per stimulus (**Figure 3E**), reflecting broad diversity in synapse strength. Since we sampled multiple $P_r$ states for each bouton, we were also able to perform quantal analysis for many of the boutons in our sample (n = 122 boutons) and calculate their RRP size. The average RRP size we measured for single boutons ($N_{sites}$ = 9.05 ± 0.63) was in good agreement with ultrastructural measurements of docked SVs in a similar preparation (10.1 ± 4.3, mean ± s.d)[32]. Assuming the average active zone contains ~10 SVs in the RRP, our approach clearly captured boutons with multiple active zones, as RRP size ranged from 1-40 release sites (**Figure 3G**). Thus, our unbiased, high-throughput approach likely captures presynapses that may be regulated within the same bouton contacting one or more postsynaptic targets. Given our access to both the number of SVs released per stimulus and RRP size, we were able to calculate the fraction of the RRP released per stimulus for single boutons (**Figure 3H**). RRP fraction trends were very similar at all boutons, suggesting that RRP fraction released per stimulus may be tightly regulated under the conditions of our cultures (**Extended Data Figure 4K**). While not demonstrated here, we expect that our technique could be used to measure RRP refilling and exhaustion during stimulus trains, another determinant of synaptic efficacy which may exhibit intersynapse variability.

Having measured diverse SV release behavior and RRP sizes across our sample of boutons, it was clear that our high-throughput approach captures substantial synaptic functional diversity. Indeed, we found that even our basic characterization of stimulus-evoked iGluSnFR3 behavior was sufficient to separate boutons into multiple functional classes (**Figure 4E**). We collected 24 basic statistics describing each bouton's stimulus-evoked iGluSnFR3 responses and projected them into two dimensions via UMAP, which clustered into three discrete functional classes. Grouping the data by functional class, we observed that the key features for classification were the magnitude of the stimulated iGluSnFR3 response at 4 mM $Ca^{2+}$ and whether boutons exhibited iGluSnFR3 activity at 0.5 mM $Ca^{2+}$. Class 1 boutons exhibited reliable activity at 0.5 mM $Ca^{2+}$ and also possessed the greatest number of release sites in their RRP ($N_{sites}$ = 14.7 ± 2.0), in contrast to Class 3 boutons which were never active at 0.5 mM $Ca^{2+}$ and possessed small RRPs ($N_{sites}$ = 4.3 ± 0.5) (**Figure 4G,H**). One potential interpretation of these data is that each functional class represents boutons at a different developmental stage. Recent work at inhibitory basket cell-Purkinje cell synapses indicated that as these synapses matured, active zones increased in size and the coupling distance between release sites and $Ca^{2+}$ channels decreased, increasing the reliability of synaptic transmission[42]. Consistent with active zone expansion, RRP size expanded by ~5 SVs per class from Class 3 to Class 1. iGluSnFR3 activity became much more probable from Class 3 to Class 1, consistent with reduced coupling distance between release sites and $Ca^{2+}$ channels. This was most obvious at 1 mM $Ca^{2+}$, where Class 3 boutons were reluctant to release glutamate ($P_{iGlu}$ = 0.19 ± 0.02), while Class 1 boutons were almost always active ($P_{iGlu}$ = 0.89 ± 0.02). Contrary to our expectations, however, the uniform $P_r$ derived from quantal analysis was nearly identical across classes for all $Ca^{2+}$. This may suggest, for instance, that the spatial relationship between release sites and $Ca^{2+}$ channels did not differ between functional classes. However, we also note that iGluSnFR3 responses at Class 1 boutons had the fastest rise and decay kinetics of the three classes, but it remains unclear how the iGluSnFR3 response kinetics are affected by the alterations in the kinetics of the underlying SV exocytosis event. If iGluSnFR3 response kinetics are proportional

to SV release kinetics, this would support a model in which Class 1 boutons are the most functionally mature of the observed bouton classes. An alternative explanation could be that Class 1 boutons are those which experience synaptic crosstalk from unlabeled boutons, but we note that labeled boutons separated by only 1.8 µm possessed distinct iGluSnFR3 activity (**Figure S2**). We expect that pairing our functional imaging and classification approach with post-hoc super-resolution immunocytochemistry of presynaptic proteins will aid the determination of the protein expression and nanostructural organizational motifs that establish synaptic functional heterogeneity.

Short-term plasticity in the presynapse critically shapes neural computation[2,43]. Depending on the input activity frequency, facilitation can occur, in which presynapses transiently increase $P_r$ to mobilize additional SVs upon stimulation[4]. Given that our high-throughput approach uncovered remarkable heterogeneity in basal glutamate properties, we probed whether we could also observe heterogeneous short-term plasticity dynamics using paired stimuli. Nearly half of boutons (49%) exhibited facilitation which decayed as ISI increased, exhibiting their largest PPR at ISI = 60 ms. However, many boutons instead preferentially facilitated only when stimulated at longer ISIs (e.g. 100, 150 ms). These divergent facilitation properties might be explained simply by RRP size or functional class, in which certain RRP sizes or functional classes give rise to specific synaptic facilitation dynamics. However, **Figure 5H-K** provides an interesting case study to the contrary. The magnitude of glutamate release (i.e. SVs released per stimulus) at these boutons was quite similar. Given that SVs released per stimulus strongly predicted functional class and RRP size (**Figure 4**), these boutons would probably fall into the same functional class. Nevertheless, their short-term plasticity behavior at 1 mM $Ca^{2+}$ was strongly divergent, suggesting that these boutons possess distinct organizations of active zone machinery. Notably, high time resolution ultrastructural analysis reveals that SVs transiently dock to the active zone membrane following an action potential[32], remaining docked for about 100 ms, potentially providing a mechanism by which presynapses could preferentially facilitate only at longer timescales. Whether the time constant for transient SV docking exhibits broad inter-bouton variation, such as seen here in the facilitation profile, is unclear. These observations motivate structure-function investigations of synapse types with diverse short-term plasticity dynamics, which we anticipate will clarify how facilitation varies between synapses and may be utilized uniquely in different circuits.

iGluSnFR3 provides direct access to glutamatergic behavior at single synapses, but the transformational potential of this technology lies also in combining iGluSnFR3 with other optical physiology reporters to access multiple physiological properties of the synapse simultaneously. For example, combining iGluSnFR3 with postsynaptic $Ca^{2+}$ imaging at single dendritic spines could reveal the patterns of glutamatergic activity which favor NMDAR activation under physiological conditions. Toward this goal, we demonstrated that co-expression of iGluSnFR3 with spine-HaloTag enabled us to directly image spontaneous glutamate release and its activation of NMDARs at single dendritic spines. Intriguingly, larger glutamate release events triggered larger NMDAR-mediated $Ca^{2+}$ flux at single spines, suggesting a dose-dependent effect of glutamate on the numbers of NMDARs activated (**Figure 6B,C**). The small amplitude iGluSnFR3 events in **Figure 6B,C** are in agreement with the spontaneous iGluSnFR3 events from **Figure 3**, suggesting that single SV release only activates a subset of NMDARs at this spine. The availability of NMDAR co-agonists like D-serine or glycine, or the NMDAR subtypes present at the synapse may play a role in this behavior[9]. Because these factors may be relevant to synaptic dysfunction in disease, high-throughput analysis of the heterogeneity of NMDAR activation across synapses will likely be particularly valuable.

## Author Contributions

S.T.B. and T.A.B. designed research; S.T.B. performed research, wrote code, and analyzed data; A.D.L., M.C.A., M.C. contributed new reagents; S.T.B., A.D.L., and T.A.B. wrote the paper.

## Acknowledgements

# Disclosure

Copyright 2024, University of Maryland, Baltimore. All rights reserved. Patent pending.



# Materials and Methods

*DNA constructs*

pAAV.CAG.iGluSnFR3.v857.GPI was a gift from Kaspar Podgorski (Addgene plasmid #178335). pEF-Synaptophysin-mRuby was a gift from Edwin Chapman (Addgene plasmid #188980). LZF97_hSyn-spine-jRGECO1a was a gift from Don Arnold (Addgene plasmid #119198). psPAX2 (Addgene plasmid #12260) and pMD2.G (Addgene plasmid #12259) were gifts from Didier Trono. pFW_iGluSnFR3 was made by subcloning the promoter and open reading frame from pAAV.CAG.iGluSnFR3.v857.GPI into pFW using NEB HIFI Assembly. LZF97_hSyn-spine-HaloTag was made by replacing the jRGECO1a-TPR3-ZFBP sequence in LZF97_hSyn-spine-jRGECO1a with HaloTag using NEB HIFI Assembly. All sequences were confirmed by whole plasmid sequencing (Plasmidsaurus) using Oxford Nanopore Technology with custom analysis and annotation.

*Lentivirus production in HEK cell culture*

Lentivirus was produced in HEK293T cells (ATCC CRL-3216) maintained in DMEM + 10% FBS and penicillin/streptomycin at 37°C and 5% $CO_2$. Cells were plated at $5 \times 10^6$ cells/10 cm plate and transfected 12-24h later with 6 μg of either pFW_iGluSnFR3 or LZF97_hSyn-spine-HaloTag + 4 μg psPAX2 + 2 μg pMD2.G using PEI for 4-6 hours. After 48h, the virus-containing media was harvested, debris removed by centrifugation at 1000 RPM for 5 min and 0.45 μm PES filtering, and single use aliquots were frozen at -80°C for long term storage.

*Rat hippocampal neuron culture and transduction*

All animal procedures were approved by the University of Maryland Animal Use and Care committee. Dissociated hippocampal cultures were prepared from E20 Sprague-Dawley rats of both sexes and plated on poly-L-lysine-coated coverslips (#1.5, 18 mm, Warner) at a density of 50,000 cells/coverslip, as previously described[39]. For experiments with iGluSnFR3 and Synaptophysin-mRuby, neurons were transfected with 1 μg of pAAV.CAG.iGluSnFR3.v857.GPI and 1 μg pEF-Synaptophysin-mRuby at DIV14-16 with Lipofectamine 2000 per manufacturer instructions. For experiments with iGluSnFR3 and spine-HaloTag, a subset of cells was infected with pFW_iGluSnFR3 and LZF97_hSyn-spine-HaloTag before plating, then plated along with uninfected cells. In this way, we were able to vary the ratio of infected cells to uninfected cells depending on the experimental requirements. We plated 10,000 dual-infected cells with 40,000 uninfected cells for a total density of 50,000 cells/well. Neurons were imaged between DIV17-23.

*Widefield and confocal microscopy*

Widefield and confocal images were acquired on a Nikon TI2 inverted microscope equipped with an Andor Dragonfly spinning disk confocal, a Plan Apo λD 60x/1.42 NA oil immersion objective. Excitation light (488/561/640 nm) was supplied by an Andor ILE and reflected to the sample through a 405/488/561/638 nm quadband polychroic (Chroma).

We recorded high-speed (200 Hz framerate) time-lapses of iGluSnFR3 activity in widefield mode, wherein the emission light bypassed the confocal unit to pass through appropriate emission filters (ET525/50, ET600/50, ET700/75 (Chroma)) to a Zyla 4.2+ sCMOS camera (Andor). 25.6 x 25.6 μm imaging regions were imaged at 20% laser power (488 nm, ~8 W/cm$^2$) with 5 ms exposures for experiments with iGluSnFR3 alone. For two-color experiments with iGluSnFR3 and spine-HaloTag, we simultaneously illuminated neurons with 488 and 640 nm laser lines. 51.2 x 51.2 μm imaging regions, with 2x2 pixel binning, were imaged at 30% laser power (488/640 nm, ~11-13 W/cm$^2$) with 20 ms exposures. The emission light was split by a 565 nm long-pass dichroic mirror to split the light from iGluSnFR3 and spine-HaloTag to two Zyla 4.2+ sCMOS cameras (Andor). For high-resolution confocal z-stacks, emission light was passed through the confocal unit to the appropriate emission filters to a Zyla 4.2+ sCMOS camera. Neurons were imaged in confocal mode at 50% laser power (488/561/640 nm, ~1-2 W/cm$^2$) with 200 ms exposures and 10 μm z-stacks (step size = 0.3 μm) were acquired using a piezo-controlled stage (ASI).

*Glutamate imaging*

For the experiments shown in **Figures 2-5**, cultured neurons co-expressing iGluSnFR3 and Synaptophysin-mRuby were imaged on DIV17-23. For imaging, neurons were transferred to an imaging chamber with parallel platinum electrodes spaced by ~1 cm and bathed in a modified Tyrode's buffer containing (in mM): 136.5 NaCl, 3 KCl, 2 $MgCl_2$, 1 $CaCl_2$, 10 D-glucose, 10 HEPES, at pH 7.4 (adjusted with 1 M NaOH) with 20 µM DNQX and 100 µM DL-AP5 to block recurrent excitation. When $[Ca^{2+}]$ was varied, NaCl was iso-osmotically substituted with $CaCl_2$ to maintain a nominal osmolarity of 308 mOsm. To help maintain temperature in the bath, the objective was heated to 37 °C with a heating collar (TOKAI HIT USA Inc., USA). In experiments with stimulus-evoked iGluSnFR3 activity, field stimuli (10 V/cm, 1 ms) were delivered by a stimulator box (S88X Square Pulse Stimulator, Grass Instrument Co., USA) triggered externally by a programmable stimulus generator (Master-8, A.M.P. Instruments, Israel). Generally, we selected 25.6 x 25.6 µm imaging regions with abundant iGluSnFR3$^+$ axonal processes and Synaptophysin-mRuby puncta; these were subjected to a battery of stimulus protocols with 20 s rest periods in between protocols. Once the protocol sequence was complete, this was repeated at the next imaging region. When we imaged spontaneous iGluSnFR3 activity, the bath solution also contained 1 µM TTX to prevent APs. We repeatedly imaged single regions for 30 s at 200 Hz (5 s rest periods in between, 6-9 trials per region) to capture spontaneously released glutamate at individual boutons.

*Simultaneous glutamate and $Ca^{2+}$ imaging*

For the experiments shown in **Figure 6**, cultured neurons co-expressing iGluSnFR3 and spine-HaloTag were prepared for imaging on DIV17-23. We achieved spine-localized $Ca^{2+}$ imaging by labeling spine-HaloTag with JF$_{646}$-BAPTA-HaloTagLigand (HTL)-AM. JF$_{646}$-BAPTA-HTL-AM was a gift from Luke Lavis[38]. We aliquoted JF$_{646}$-BAPTA-HTL-AM as a 1 mM stock in anhydrous dimethyl sulfoxide (DMSO) and stored at -80 °C.

To treat cells with JF$_{646}$-BAPTA-HTL-AM, we followed a protocol similar to what has been previously described by Bradberry et al. 2021[44]. Conditioned media (3x300 µL) was transferred from a well containing a coverslip with cultured neurons to an empty 12-well plate. For each experiment, we made a working stock of JF$_{646}$-BATPA-HTL-AM diluted in a modified Tyrode's buffer with the following composition (in mM): 136.5 NaCl, 3 KCl, 2 $MgCl_2$, 1 $CaCl_2$, 10 D-glucose, 10 HEPES and 2 µM JF$_{646}$-BAPTA-HTL-AM. For each coverslip incubation, we added 300 µL of the JF$_{646}$-BAPTA-HTL-AM working stock to a well with 300 µL of conditioned media, for a 1 µM effective dye concentration during incubation.

Coverslips of cultured neurons were transferred to the dye-containing wells and incubated for 30 minutes at 37 °C. Following incubation, coverslips were immediately transferred sequentially to the other two wells with conditioned media to wash off free JF$_{646}$-BAPTA-HTL-AM before being returned to their original 12-well plate for recovery. Neurons were allowed to recover from the dye incubation for 30-60 minutes at 37 °C. For imaging, neurons were transferred to an imaging chamber (Warner Instruments, USA) and bathed in a modified Tyrode's buffer containing (in mM): 135 NaCl, 3 KCl, 4 $CaCl_2$, 0 $MgCl_2$, 10 D-glucose, 10 HEPES, 1 Trolox (to preserve fluorescence of JF$_{646}$-BAPTA-HTL-AM), and 1 µM TTX in a climate-controlled chamber (37 °C, 100% humidity, TOKAI HIT USA Inc., USA). Spontaneous glutamate release and subsequent NMDAR-mediated $Ca^{2+}$ flux at single dendritic spines were observed for 20 s at 50 Hz before moving to another imaging region or washing in solution containing 100 µM DL-AP5. After wash-in, imaging of the same regions was repeated.

*Hardware automation*

As described by **Figure 1A**, we developed a hardware automation scheme to fully automate imaging experiments, improving throughput/reproducibility. A custom *Python* script enabled control of the microscope and stage (i.e. imaging positions), image acquisition, electrical stimulation, and solution exchange.

The microscope and stage piezo were controlled from the script via the Andor (Oxford Instruments) REST API and Fusion software. This approach allowed us to store stage positions of multiple regions in a Python list object and iterate protocols over chosen imaging regions. We developed custom functions to automate updates to key imaging parameters (e.g. camera settings, filenames, focus stabilization) throughout the protocol, enabling more complex and robust automated imaging sequences.

Electrical field stimulation was controlled via the Master-8 and S88x Square Pulse Stimulator. At the beginning of each imaging protocol with electrical stimulus, we first established USB serial communication with

563 the Master-8. To automatically update stimulus paradigms, we used a dictionary data structure to link stimulus
564 paradigm parameters to imaging protocols – this enabled us to pre-configure the Master-8 prior to each imaging
565 protocol to deliver diverse stimulus paradigms (e.g. single stimuli, paired stimuli, stimulus trains). To trigger
566 stimulation during imaging, we predefined the frame in each imaging protocol (Fusion) during which a TTL pulse
567 would be sent via BNC cable to the Master-8. After receiving the TTL from the microscope, the Master-8 triggered
568 field stimulus of neurons by sending its pulse sequence via BNC cable to the S88X Square Pulse Stimulator.

569      The workflow was similar for solution exchange. Sub-functions established USB serial communication
570 with a ValveLink8.2 Controller (AutoMate Scientific), which allowed us to toggle pinch valves on a gravity flow
571 perfusion apparatus, initiating fluid flow. To achieve fluid exchange, we simultaneously triggered an Arduino
572 microcontroller (Arduino, Italy) which controlled a peristaltic pump, vacuuming excess fluid from the imaging
573 chamber[45]. The gravity flow perfusion apparatus was adjusted to a flow rate of ~1.5 mL/min.
574

575 *Image segmentation and extraction of intensity-time traces*
576      At the end of each iGluSnFR3 imaging session, confocal z-stacks were recorded of the same imaging
577 fields to capture the position of Synaptophysin-mRuby puncta (i.e. putative boutons) along the axonal arbor.
578 Most confocal z-stack image processing was performed with custom macros in FIJI as we have previously
579 described[46]. Briefly, the middle 3.33 μm of each z-stack were extracted and converted to maximum intensity
580 projections to eliminate putative boutons outside the widefield imaging plane. Background subtraction was
581 performed by identifying the lowest 1% of pixel intensity per channel and subtracting this value from its respective
582 image channel. We constructed a mask of the axonal arbor by automatically thresholding the iGluSnFR3 channel
583 on the top 5% of pixel intensities. Binary axonal arbor masks were smoothed and small background particles
584 were removed. Putative synaptic puncta were identified in the Synaptophysin-mRuby channel with the plugin
585 SynQuant. Only Synaptophysin-mRuby ROIs within the boundary of the mask of the axonal arbor were analyzed.
586 After drift correcting for small stage movements between perfusion rounds at single imaging regions, we
587 distributed the "ROI maps" to folders containing individual imaging trials. A custom FIJI macro iterated through
588 all subdirectories, opening videos and applying their respective ROI maps, populating a separate directory with
589 .csv files of the intensity-time recordings at each ROI, which we then read into *R* for analysis.

590      For activity-based segmentation, we applied a method described in Mendonca et al. 2022[23] with some
591 modifications. Briefly, a moving average filter with a 5-point span was used to smooth the temporal profile of the
592 iGluSnFR3 responses. A band-pass Gaussian filter (0.05-200 Hz) was then applied to amplify the iGluSnFR3
593 signal. At each pixel we subtracted the mean value and divided by the standard deviation, which had the effect
594 of suppressing inactive stretches of the axonal arbor and amplifying active stretches (the "activity footprint" of
595 the axon). From these, we created max intensity projections which were thresholded on the top 3% of all pixels
596 to generate ROI maps of activity along the axonal arbor. We applied these "activity maps" to their respective
597 videos and extracted .csv files of intensity-time recordings for each ROI, which we then read into *R* for analysis.
598

599 *Fluorescence signal extraction*
600      To normalize iGluSnFR3 intensity-time traces to ΔF/F, correct baseline fluctuations, and extract
601 fluorescence signals at scale, we wrote a custom algorithm in *R* (*peakFinder.R*). The algorithm proceeds in three
602 stages, iteratively refining its approximation of the trace's baseline. First, the algorithm flagged outlier indices as
603 those which rise above a threshold of σ (standard deviation) from the rolling median (0.75 s span) of the raw
604 fluorescence intensity (median filter). Once a first approximation of the outliers is known, a more refined
605 approximation of the baseline, F, was made on the raw intensity trace using a rolling median (0.75 s span) which
606 excluded the known outlier indices. The outlier indices were replaced with the last non-NA value (i.e. known
607 intensity at non-signal indices) using a "last observation carried forward" function in *R* (*na.locf*()).Then, traces
608 were adjusted to ΔF/F by dividing the raw intensity by the approximate baseline. Using a Schmitt trigger
609 thresholding approach, we identified putative fluorescence signals when they exceeded an upper threshold of
610 3.5σ; the signals terminated when they decayed below a lower threshold of 1.5σ; the indices corresponding to
611 these putative fluorescence signals were flagged. To identify the full extent of putative fluorescence signals and
612 properly exclude them from the baseline approximation, additional points before and after putative fluorescence
613 signals were flagged as signal indices according to the known rise and decay kinetics of the fluorescent sensor

being imaged. With the original outliers and the putative signal indices flagged, a new baseline (F) was calculated from the rolling average of the raw intensity trace excluding outliers and putative signals, and the final iteration of ΔF/F was calculated. The final detection of fluorescence transients was achieved with a more stringent threshold (lower, 1.5σ, upper, 5σ) and annotated for further analysis.

For the experiments in **Figure 6**, we found that the slower kinetics of $JF_{646}$ and the frequent convolution of $JF_{646}$ transients with one another made it difficult to approximate the baseline and accurately convert traces to ΔF/F using a median filter. Instead, we used a percentile filter approach, wherein the trace was divided into 10 equivalent time bins (e.g. 0-2 s, 2-4 s, etc.), and indices which comprised the bottom 30% of intensity values were identified in each bin. Similar to above, these were flagged as putative baseline indices, and the baseline fluorescence intensity at these indices were interpolated using *na.locf()*. A rolling average of these points with a 0.75 s span was calculated to approximate the baseline. The trace was then adjusted to ΔF/F, and putative signals identified with a Schmitt trigger (lower, 1.5σ, upper, 3.5σ). We then repeated this process with the putative signals being excluded from the percentile filter. The final iteration of ΔF/F was calculated and $JF_{646}$ transients were once again identified with a stringent threshold (lower, 1.5σ, upper, 5σ) and annotated for further analysis.

*Analysis of single stimulus-evoked and spontaneous iGluSnFR3 transients*

Annotated iGluSnFR3 transients from stimulus-evoked and spontaneous recordings were analyzed using custom analysis scripts in *R*. We measured the peak ΔF/F of found transients, and for stimulus-evoked transients, we calculated the time delay (Δt) between the stimulus and the peak ΔF/F to measure the speed with which iGluSnFR3 reports stimulus-secretion coupling. To measure the rise time, $t_{rise}$, we established a time cutoff of corresponding to the time of stimulus, prior to the time of peak ΔF/F. We then found the minimum ΔF/F prior to the peak maximum, and solved for the slope of a line between the minimum ΔF/F and the peak ΔF/F. From the peak ΔF/F, we established the 10% and 90% fluorescence levels for each transient and calculated the $t_{rise}$ between these two points based on the found rise slope for each transient. To measure the decay time constant, $\tau_{decay}$, for each iGluSnFR3 transient, we used the package *nlstools*[47] to fit an exponential decay function, $f(t) = Ae^{-t/\tau_{decay}}$ from the peak ΔF/F to the end of the annotated transient. From the calculated values for the pre-exponential factor, $A$, and $\tau_{decay}$, we calculated the decay time from 90% to 10% of the peak ΔF/F, $t_{decay}$. Similarly, to calculate the full-width at half-maximum ($t_{1/2}$) of each transient, we used the 50% ΔF/F value for each peak to solve for the time of 50% ΔF/F on the peak rise (linear fit) and the peak decay (exponential decay fit), and subtracted these values to generate $t_{1/2}$. The procedure was identical for spontaneous iGluSnFR3 transients, except for the calculation of $t_{rise}$. Since there was no stimulus to mark the beginning of an iGluSnFR3 transient, we established our time cutoff as 25 ms prior to the peak ΔF/F (informed by the published rise kinetics of iGluSnFR3, ~19 ms[18]). Otherwise, peak statistics were measured identically (omitting Δt, which could not be calculated). For both stimulus-evoked and spontaneous transients, signals were filtered out of the dataset if $\tau_{decay}$ < 15 ms or $\tau_{decay}$ > 300 ms, as we determined these represented spurious, high-frequency noise or non-glutamate release activity (e.g. iGluSnFR3$^+$ vesicle trafficking through the axon, which had a characteristically slow time constant uncoupled from the stimulus), respectively.

We calculated several properties of boutons from our stimulus-evoked iGluSnFR3 trials. The probability of observing an iGluSnFR3 transient ($P_{iGlu}$) was defined as a binary for each trial: 1 if a signal was detected, or 0 if there was no signal detected. The sum of these binary values was divided by the total number of trials to define $P_{iGlu}$ for an ROI at a single $[Ca^{2+}]_{bath}$. To assess whether the stimulus-evoked glutamate release was mono- or multivesicular, we compared the average peak ΔF/F of stimulus-evoked iGluSnFR3 transients for each ROI ($E_{\Delta F/F}$) to the average peak ΔF/F of spontaneous iGluSnFR3 transients at each $[Ca^{2+}]_{bath}$ ($S_{\Delta F/F}$, see **Figure 3**), which represented putative single vesicle glutamate release events. When the value of the derived metric $E_{\Delta F/F}/S_{\Delta F/F}$ was >1, we interpreted this as the release of multiple vesicles (but see *Discussion*). The coefficients of variation (CVs, mean / σ) were calculated for all statistics at each ROI. For pair-wise comparisons, we calculated statistical significance via Kolmogorov-Smirnov and Mann-Whitney-Wilcoxon tests. To compare statistics across $[Ca^{2+}]_{bath}$, we calculated one-way analysis of variance (ANOVA).

*Mean-variance analysis of iGluSnFR3 transients*

To perform mean-variance analysis (MVA) of iGluSnFR3 transients, we sampled the single action potential (AP)-evoked iGluSnFR3 activity at individual boutons across multiple $[Ca^{2+}]_{bath}$ (sampling multiple $P_r$ states). To accurately measure the mean and the variance of the iGluSnFR3 ΔF/F for each stimulus, we used an approach that was agnostic to the algorithmic definition of an iGluSnFR3 signal. The maximum of the iGluSnFR3 ΔF/F was measured in a time window starting from the stimulus (t = 0) and extending to 250 ms post-stimulus. This enabled measurement of sub-threshold maxima and noise, especially at 0.5 mM $Ca^{2+}$, where most boutons were quiescent. We then converted the measured amplitudes to $E_{ΔF/F}/S_{ΔF/F}$ and measured their variance. Each bouton possessed four data points of the form (x, y) corresponding to (mean, variance) at each $[Ca^{2+}]_{bath}$, and each bouton was fit using the uniform probability binomial model of the form: $\sigma^2 = Q\overline{x} - \overline{x}^2/N_{sites}$[28]. In fitting the binomial model, $N_{sites}$ was constrained to positive values < 100 and $Q$ was constrained to values between 0.8-1.2, as $E_{ΔF/F}/S_{ΔF/F} = 1$ was expected to represent the iGluSnFR3 response due to a single vesicle, per the analyses in **Figure 3**.

Boutons were accepted for analysis if the sum of the squared residuals was ≤ 1 and their maximum $P_r$ > 0.45[14]. From the binomial model, we calculated the following synaptic parameters: the uniform release probability ($P_r$) at each $[Ca^{2+}]_{bath}$, the quantal size of the iGluSnFR3 response ($Q$), and the total number of release sites in the readily releasable pool ($N_{sites}$).

*Generating a UMAP representation of bouton physiology*

To cluster boutons into functionally distinct classes (**Figure 4**), we calculated a collection of statistics which summarized the intrinsic behavior of boutons during single AP trials. First, only iGluSnFR3 transients which exceeded our threshold of detection (see above, *Fluorescence signal extraction*) were used for calculating summary statistics. The probability of observing an iGluSnFR3 transient, $P_{iGlu}$, was the ratio of the number of transients identified at a given bouton to the number of single stimulus trials administered. Transients were only counted toward $P_{iGlu}$ if a transient maximum occurred within 500 ms of a preceding stimulus. $P_{iGlu}$ was calculated per bouton for each $[Ca^{2+}]_{bath}$. We also calculated the mean amplitude and the variance for iGluSnFR3 transients in terms of $E_{ΔF/F}/S_{ΔF/F}$ at each $[Ca^{2+}]_{bath}$. Because the mean and variance were often unavailable for boutons which possessed no identifiable iGluSnFR3 transients at 0.5 mM $Ca^{2+}$, boutons with *NA* were coerced to 0 for the purposes of the analysis.

For the remaining statistics, we restricted our analysis to $[Ca^{2+}]_{bath}$ = 1, 2, or 4 mM, as data was too sparse to calculate coefficients of variation (CVs) at 0.5 mM $Ca^{2+}$. We calculated the mean decay time constant, $\tau_{decay}$, as well as the CV of peak ΔF/F, CV of $\tau_{decay}$, and CV of Δt. The mean Δt was omitted as it exhibited little variation in magnitude across boutons (unlike mean amplitude and mean $\tau_{decay}$).

For all statistics (except for $P_{iGlu}$, which was already normalized between 0 and 1), missing values were coerced to 0 and the values in each column were normalized between 0 and 1, equally weighting all of the statistics in the data matrix. This resulted in 24 data columns (each $[Ca^{2+}]_{bath}$ constituted an additional observation for each of the 7 summary statistics). We used the *umap* and *dbscan* libraries in *R* to generate UMAP scores for the data matrix and cluster the UMAP score output (DBSCAN minimum points per cluster = 10). Cluster identities were re-associated with their original bouton IDs, which enabled us to categorize our bouton physiology data according to their UMAP class. Grouping the data in this way allowed us to visualize the defining characteristics of each bouton class (**Figure 4E-H**).

*Analysis of iGluSnFR3 transients evoked by paired stimuli*

The protocol for the paired pulse experiment in **Figure 5** was administered with each protocol in triplicate. The protocol sequence began with a Test Pulse (a single stimulus), followed by paired pulses with inter-stimulus intervals (ISIs) of 60, 75, 100, 150, or 500 ms. There was a 20 s recovery period between each trial. This protocol sequence was first administered in a bath solution with 0.5 mM $Ca^{2+}$. In between iterations of the protocol sequences, buffer solution containing 1 mM $Ca^{2+}$ or 2 mM $Ca^{2+}$ was washed in.

We averaged the responses from the three Test Pulse trials to generate the average response to a single stimulus for each ROI and each $[Ca^{2+}]_{bath}$ measured. We aligned the average response to the test pulse to the first stimulus in each paired pulse recording and subtracted the test pulse from the paired pulse recording,

715 enabling more accurate measurement of the amplitude of the 2nd iGluSnFR3 transient (see **Figure 5B**). This was
716 especially important in cases where a short ISI resulted in a convolution of the two iGluSnFR3 transients (e.g.
717 ISI = 60, 75, or 100 ms).
718      We performed this operation for every ROI in the dataset and then divided the traces into two stimulus
719 epochs: the first stimulus epoch began at the first stimulus and ended at the second stimulus; the second stimulus
720 epoch began with the second stimulus and terminated 500 ms later. For each trial, we identified the amplitude
721 of the first pulse ($Pulse_1$) as the maximum ΔF/F within the first stimulus epoch of the unmodified trace. To
722 determine the amplitude of the second pulse ($Pulse_2$), we identified the maximum ΔF/F within the second
723 stimulus epoch in the subtracted trace. To eliminate noise from the measurement, we only retained amplitudes
724 which exceeded the value of the average spontaneous transient amplitude (see **Figure 3, Figure 4B**). Paired
725 pulse ratios were then calculated for each trial.
726
727 *Analysis of simultaneous iGluSnFR3 and $JF_{646}$-BAPTA-AM recordings*
728      We segmented simultaneous recordings of iGluSnFR3 and $JF_{646}$-BAPTA-HTL-AM on the activity in the
729 iGluSnFR3 channel as described above. These iGluSnFR3 activity maps were distributed to folders containing
730 the recording for either the iGluSnFR3 or $JF_{646}$ channel and intensity-time traces were extracted as before.
731 Because the ROI maps were identical between channels of the same recording, we were able to pair the traces
732 by ROI in *R*. To characterize putative synaptic transmission events (paired iGluSnFR3/$JF_{646}$ signals), we took
733 advantage of our robust peak discrimination in the iGluSnFR3 channel. Around each iGluSnFR3 signal identified
734 by our peak finding algorithm, we defined a temporal window in which to search for a local maximum in the $JF_{646}$
735 channel (**Figure 6**). The lower boundary of the temporal window was 10 ms prior to the iGluSnFR3 peak
736 maximum, and the upper boundary of the temporal window was 250 ms after the iGluSnFR3 peak maximum. In
737 this way, we were able to pair the local maxima (which reflected the peak of paired $Ca^{2+}$ transients) in each
738 channel for bona fide glutamate release events, which could then be analyzed.
739      To discriminate putative transmission events from noise, we took advantage of the output from our peak
740 finding algorithm, which tabulates putative baseline indices as part of the baseline adjustment routine. For each
741 dendritic spine in the dataset, we selected all of the putative baseline indices for the $JF_{646}$-BAPTA channel and
742 calculated the standard deviation of these points. A signal threshold of 3.5σ was set for each spine, and $JF_{646}$-
743 BAPTA signals above this threshold were considered transmission.
744
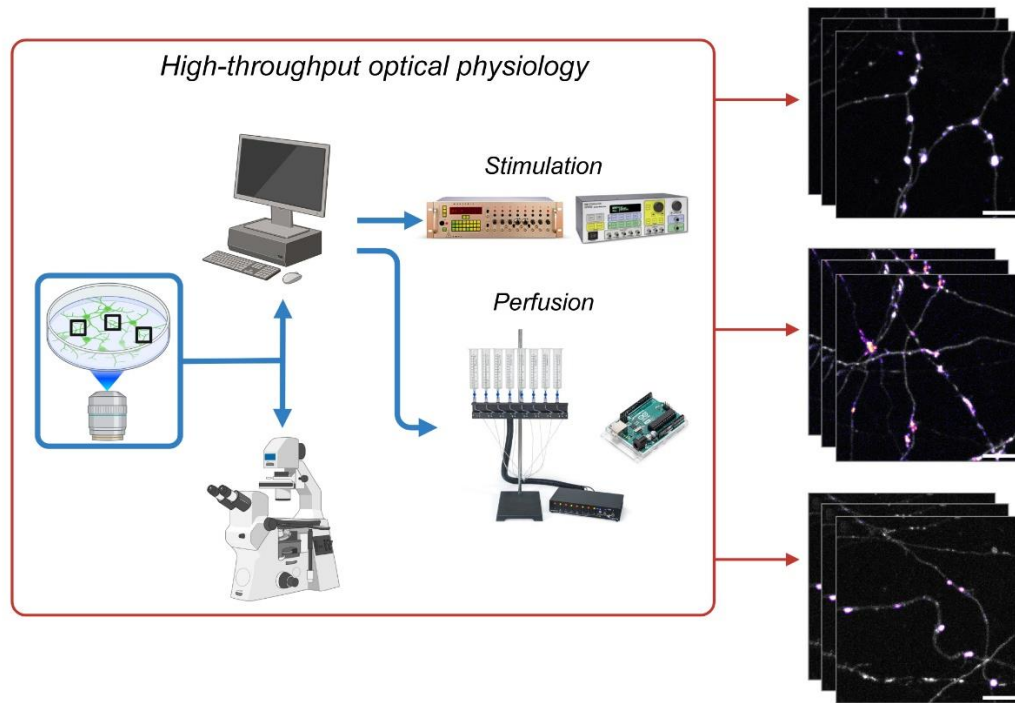745 *Data Visualization*
746      All data analysis and visualization was carried out using custom scripts in *R*. In general, we relied on
747 structured data frames with several string variables by which data could be sorted and analyzed. Figures were
748 plotted using a combination of the packages *ggplot2* and *gridExtra*.
749      For the maps of synaptic function in **Figure 4-6**, we used a custom workflow and the packages
750 *RImageJROI* and *EBImage*. First, we generated .png files of the max-projected confocal z-stacks for individual
751 imaging regions. These .png files were read into *R* as raster objects. Zip files containing the ROI information
752 were generated for each imaging region in *FIJI*. Using *RImageJROI*, we were able to read the .zip files into *R*.
753 Using *ggplot2*, we layered the ROI polygons from *FIJI* on top of the raster of the imaging region. Statistics could
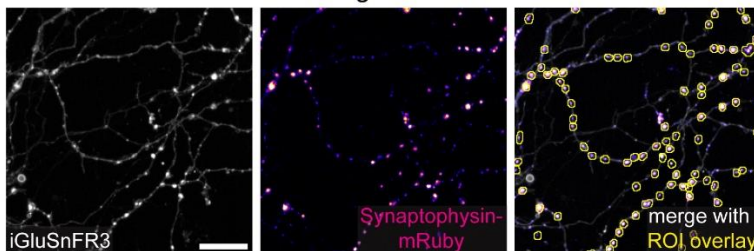754 then be assigned to each ROI polygon on the basis of their unique ROI identity.
755
756 *Statistics*
757 Statistical analyses were performed in *R*. Statistical differences between datasets were tested with pair-wise
758 Mann-Whitney-Wilcoxon and Kolmogorov-Smirnov tests. For datasets with multiple groups, data were also
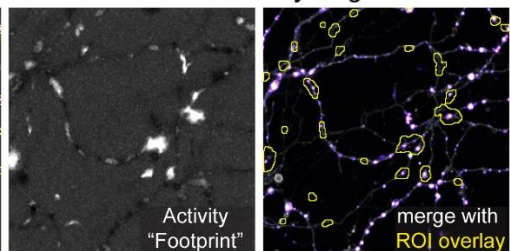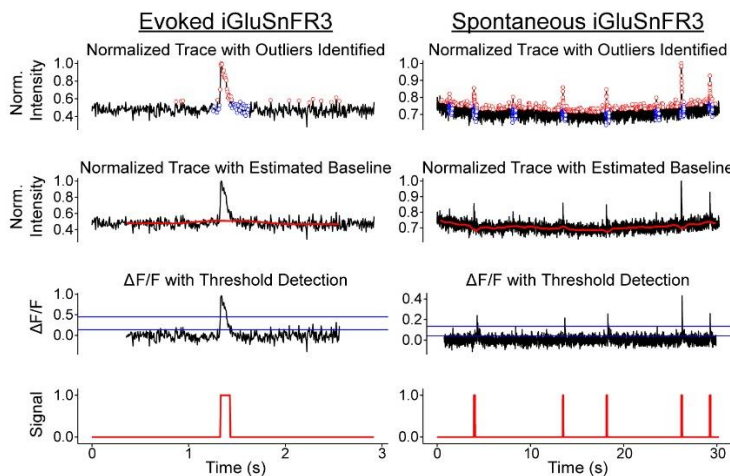759 tested with one-way ANOVA.
760

**A** High-throughput optical physiology

**B** *Fluorescent marker segmentation*

iGluSnFR3 · Synaptophysin-mRuby · merge with ROI overlay

**C** *iGluSnFR3 activity segmentation*

Activity "Footprint" · merge with ROI overlay

**D** *Automatic ΔF/F calculation and signal extraction*

Evoked iGluSnFR3 · Spontaneous iGluSnFR3

Normalized Trace with Outliers Identified

Normalized Trace with Estimated Baseline

ΔF/F with Threshold Detection

**E** *iGluSnFR3 transient analysis*

Stimulus · 90% · 10%

— Signal
— Baseline
— Exp. Decay Fit
● $t_{rise}$
● $t_{decay}$
◆ $t_{1/2}$
◆ $Peak_{ΔF/F}$

1 ΔF/F · 100 ms
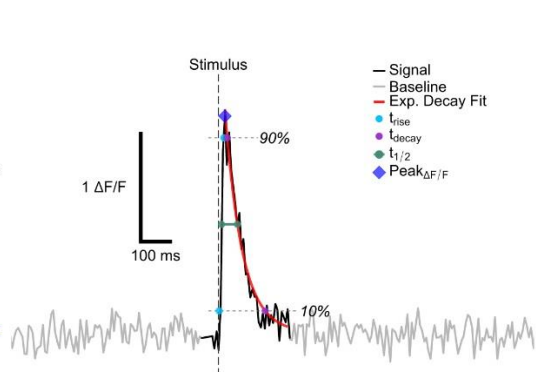
**Figure 1**. **An end-to-end framework enables high-throughput measurement of presynaptic function with iGluSnFR3. A)** An automated imaging approach using custom Python scripts enables high-throughput optical physiology of presynaptic boutons. Python routines control the microscope, triggering imaging protocols, and controlling stage positions via a REST API (Andor, Oxford Instruments). Python sub-routines configure a programmable stimulus generator. Whenever an imaging protocol triggers a TTL pulse to the programmable stimulus generator, the pre-configured stimulus paradigm is sent to an electrical stimulator which stimulates neurons via parallel platinum wire electrodes. Other Python sub-routines toggle pinch valves on a gravity flow perfusion apparatus are simultaneously with an Arduino-controlled vacuum to permit fluid exchange. The result is a versatile, automated approach to experimental design that dramatically improves reproducibility and throughput for assays of synapse physiology with iGluSnFR3. At right are imaging regions of axons expressing iGluSnFR3 (gray LUT) and Synaptophysin-mRuby (fire LUT), a marker for the presynaptic bouton. Scale bar = 5 µm. **B,C)** Time-lapse recordings of iGluSnFR3 activity along axons can be batch segmented based on a fluorescent marker (**B**) or iGluSnFR3 activity (**C**). Scale bar = 10 µm. **D)** A custom R algorithm automatically identifies the baseline, calculates ΔF/F, and extracts putative iGluSnFR3 signals. The algorithm's output for two exemplar regions-of-interest (ROIs) are shown. Left, stimulus-evoked iGluSnFR3 activity; right, spontaneous, AP-independent iGluSnFR3 transients. **E)** Extracted iGluSnFR3 transients can be analyzed for several intrinsic peak parameters: peak ΔF/F, exponential decay time constant ($\tau_{decay}$), full-width at half-maximum ($t_{1/2}$), 10-90% rise time ($t_{rise}$), 90-10% decay time ($t_{decay}$), and for stimulus-evoked transients, the time interval between peak and stimulus onset ($\Delta t$).

807
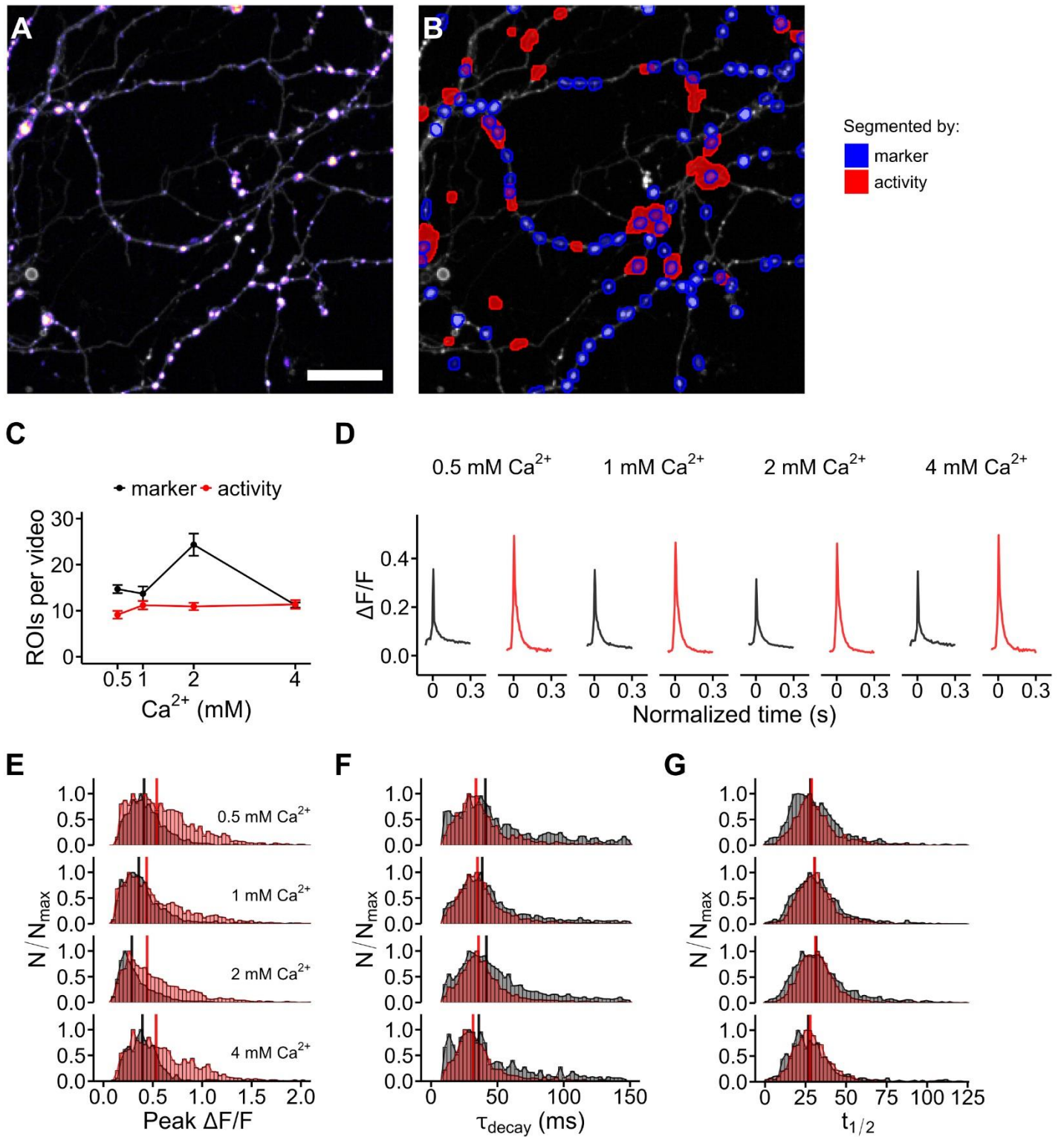


808
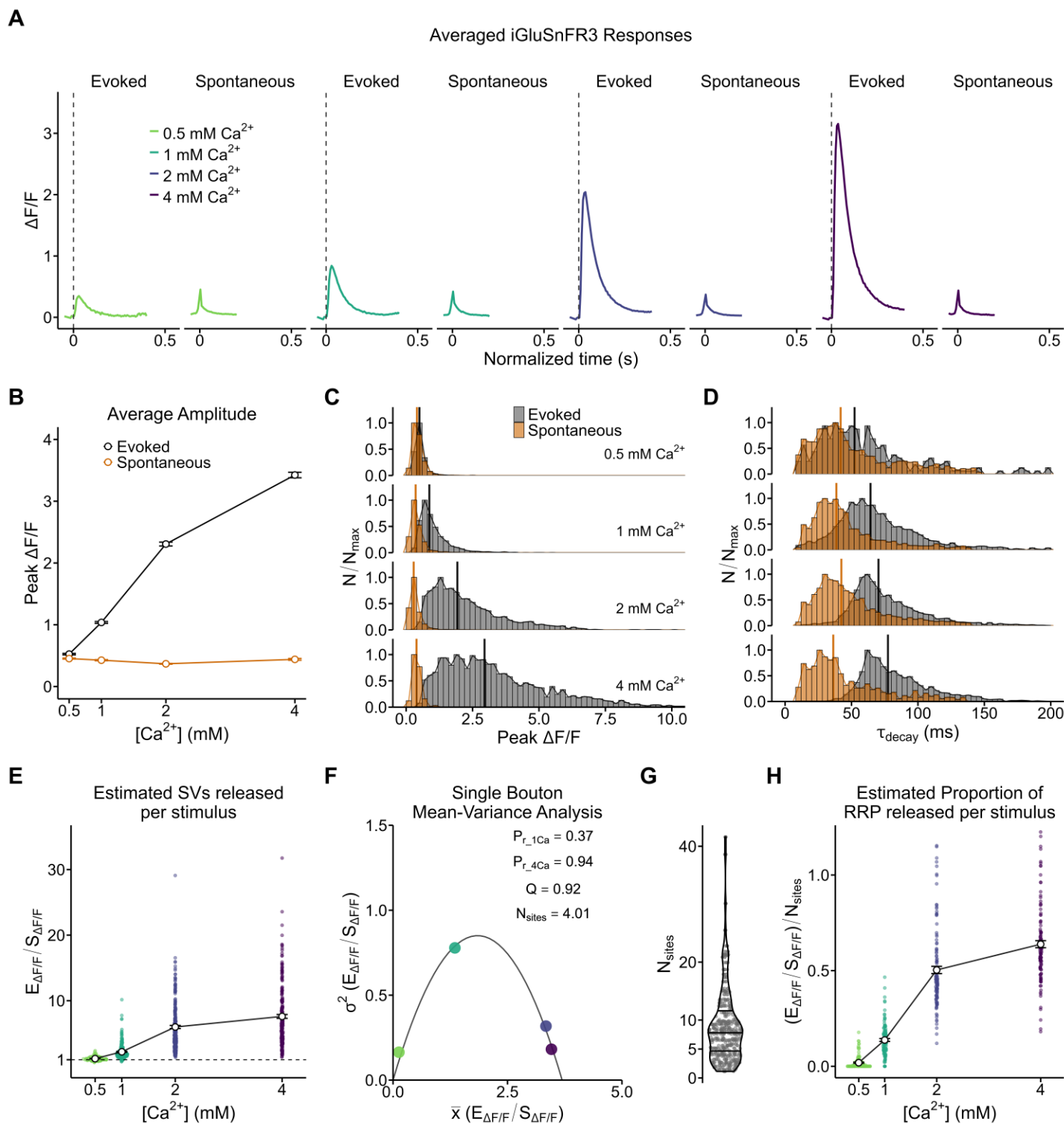
809

810

811

812

**Figure 2. Spontaneous, quantal iGluSnFR3 activity at single synapses is captured by marker- and activity-based segmentation. A)** An exemplar imaging region (51.2 x 51.2 μm) with an axon co-expressing iGluSnFR3 (grey LUT) and Synaptophysin-mRuby3 (fire LUT). Scale bar = 10 μm. **B)** Spatial map of batch segmented ROIs according to Synaptophysin-mRuby3 expression (blue) or detected iGluSnFR3 activity (red) at $[Ca^{2+}]_{bath}$ = 2 mM for one trial. The segmentation comparison indicates that several boutons marked by Synaptophysin-mRuby3 encompass true glutamate release sites, though many more boutons tended to be silent during the 30 s recording period. **C)** The number of ROIs detected per imaging region depended on the segmentation method. **D)** The average AP-independent, spontaneous iGluSnFR3 transients at each $[Ca^{2+}]_{bath}$ for either segmentation method. For both methods, the shape and amplitude of the average iGluSnFR3 transient was similar across all $[Ca^{2+}]_{bath}$, supporting the notion that spontaneous iGluSnFR3 activity represents single vesicle release. **E)** Normalized histogram of peak ΔF/F collected via marker or activity segmentation across $[Ca^{2+}]_{bath}$. **F)** Normalized histogram of $\tau_{decay}$. **G)** Normalized histogram of $t_{1/2}$. For **E**, **F**, and **G**, vertical lines indicate the medians of the distributions. Detected iGluSnFR3 transients were persistently larger in amplitude with faster $\tau_{decay}$ when extracted via activity segmentation.

**A**



**B** Average Amplitude

**C**

**D**

**E** Estimated SVs released per stimulus

**F** Single Bouton Mean-Variance Analysis

$P_{r\_1Ca} = 0.37$
$P_{r\_4Ca} = 0.94$
$Q = 0.92$
$N_{sites} = 4.01$

**G**

**H** Estimated Proportion of RRP released per stimulus

850

**Figure 3. Estimating the number of vesicles released during evoked SV release. A)** The averaged iGluSnFR3 response for stimulus-evoked and spontaneous glutamate release across $[Ca^{2+}]_{bath}$ = 0.5, 1, 2, or 4 mM, incorporating the marker-based segmentation data from **Figure 2**. Dashed vertical lines indicate stimulus. **B)** Scatterplot of average peak amplitude (peak $\Delta F/F$) vs. $[Ca^{2+}]_{bath}$ for stimulus-evoked and spontaneous iGluSnFR3 transients. **C)** Normalized histogram of peak $\Delta F/F$ comparing identified spontaneous (orange) with stimulus-evoked (black) iGluSnFR3 transients at each $[Ca^{2+}]_{bath}$. At 0.5 mM $Ca^{2+}$, the distribution of spontaneous and stimulus-evoked iGluSnFR3 transients largely overlap, suggesting that at this low $[Ca^{2+}]_{bath}$, putative boutons only release a single vesicle in response to stimulus. At 2 and 4 mM $Ca^{2+}$, boutons transition to multivesicular release. **D)** Normalized histogram of $\tau_{decay}$. In **C, D,** black and orange vertical lines indicate median values of the distributions for stimulus-evoked and spontaneous iGluSnFR3 transients, respectively. **E)** Scatterplot of the $E_{\Delta F/F}/S_{\Delta F/F}$ vs. $[Ca^{2+}]_{bath}$. $E_{\Delta F/F}/S_{\Delta F/F}$ is the peak $\Delta F/F$ of stimulus-evoked iGluSnFR3 transients ($E_{\Delta F/F}$) normalized to the population average of the peak $\Delta F/F$ of spontaneous iGluSnFR3 transients ($S_{\Delta F/F}$) at each respective $[Ca^{2+}]_{bath}$. Colored dots indicate the mean value of $E_{\Delta F/F}/S_{\Delta F/F}$ at individual boutons. The responses at 0.5 mM $Ca^{2+}$ cluster around $Evoked_{\Delta F/F}/Spont_{\Delta F/F}$ = 1 (horizontal dashed line), indicating univesicular release at this $Ca^{2+}$. **F)** Scatterplot of variance ($\sigma^2$) of $E_{\Delta F/F}/S_{\Delta F/F}$ vs. mean ($\bar{x}$) $E_{\Delta F/F}/S_{\Delta F/F}$ for an exemplar bouton. Mean-variance distributions were fit with a binomial of the form $\sigma^2 = Q\bar{x} - \bar{x}^2/N_{sites}$, where $Q$ is the single vesicle iGluSnFR3 response and $N_{sites}$ is the total number of release sites at each bouton (i.e. the readily releasable pool, RRP). From the fitted binomial, we extracted the uniform release probability at each release site, $P_r$, for each $[Ca^{2+}]_{bath}$. The $P_r$ for 1 and 4 mM $Ca^{2+}$, as well as the solved values for $Q$ and $N_{sites}$ are shown on the plot. **G)** A violin plot of the distribution of solved $N_{sites}$ per bouton. The behavior of 122/244 boutons in our dataset could be well-described by a binomial fit. **H)** Scatterplot of $(E_{\Delta F/F}/S_{\Delta F/F})/N_{sites}$ vs. $[Ca^{2+}]_{bath}$. As the value of $E_{\Delta F/F}/S_{\Delta F/F}$ was a proxy for the total number of vesicles released per stimulus, the ratio of $E_{\Delta F/F}/S_{\Delta F/F}$ to $N_{sites}$ permitted us to estimate the proportion of the RRP mobilized per stimulus at each bouton across $[Ca^{2+}]_{bath}$.

851

852

853
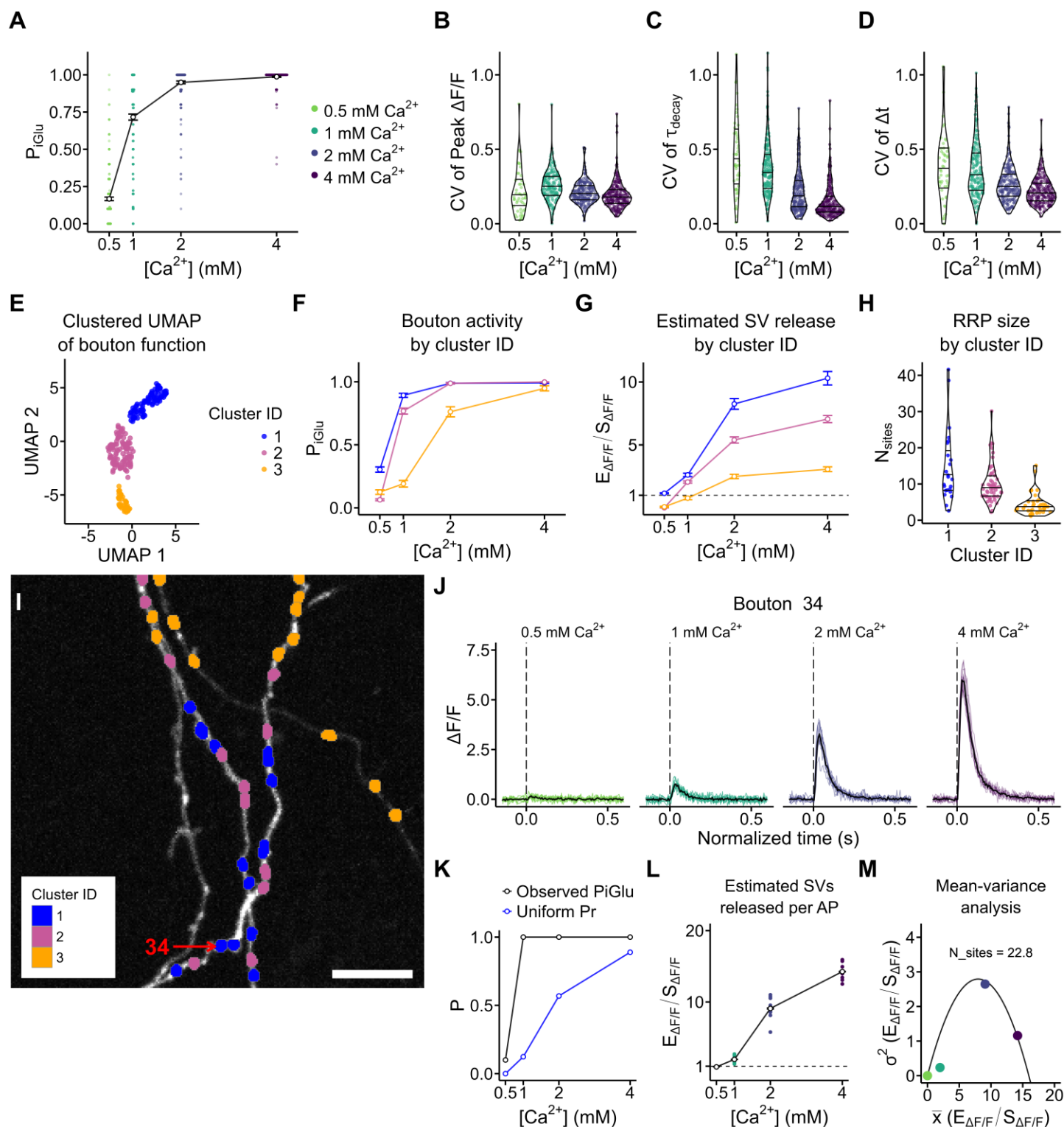
**Figure 4. Tracking stimulus-evoked iGluSnFR3 activity at individual boutons captures heterogeneous bouton behavior that can be separated into three functional classes. A)** The probability of measuring a stimulus-evoked iGluSnFR3 transient ($P_{iGlu}$) was calculated at putative boutons across all $[Ca^{2+}]_{bath}$. The trend line indicates the mean ± S.E.M. **B)** The coefficient of variation (CV) of the peak ΔF/F for measured iGluSnFR3 transients. Each colored dot in the violin plots indicates the value of $CV_{ΔF/F}$ for a single bouton. **C)** CV of $\tau_{decay}$. **D)** CV of Δt. **E)** UMAP representation of statistics of iGluSnFR3 activity at 251 boutons. DBSCAN of the UMAP indicate that there are three classes of boutons. **F-H)** By grouping the data according to cluster identity, we identified defining features of each bouton grouping. **F)** $P_{iGlu}$ vs. $[Ca^{2+}]_{bath}$ grouped by cluster ID. **G)** Estimated number of SVs released ($E_{ΔF/F}/S_{ΔF/F}$) vs. $[Ca^{2+}]_{bath}$. **H)** Estimated RRP size ($N_{sites}$) vs. cluster ID. **I)** An exemplar imaging region with each bouton color coded by cluster ID. **J-M)** Targeted functional analysis of Bouton 34. **J)** Averaged iGluSnFR3 waveform of single AP trials for Bouton 34. The individual trial responses are color-coded by $[Ca^{2+}]_{bath}$ with the averaged response in black. **K)** The observed $P_{iGlu}$ (black) and the calculated uniform $P_r$ (blue) vs. $[Ca^{2+}]_{bath}$. **L)** The $E_{ΔF/F}/S_{ΔF/F}$ curve for Bouton 34 vs. $[Ca^{2+}]_{bath}$, with individual trial values color-coded by $[Ca^{2+}]_{bath}$. **M)** Scatterplot of variance ($\sigma^2$) of $E_{ΔF/F}/S_{ΔF/F}$ vs. mean ($\bar{x}$) $E_{ΔF/F}/S_{ΔF/F}$ for Bouton 34. The colored dots indicate the measured $\sigma^2$ and $\bar{x}$ at each $[Ca^{2+}]_{bath}$, while the black curve indicates the binomial fit.

854

855

856

857

858

859

860

861

862

863

864

865

866

867

868

869

870

871

872

873

874

876
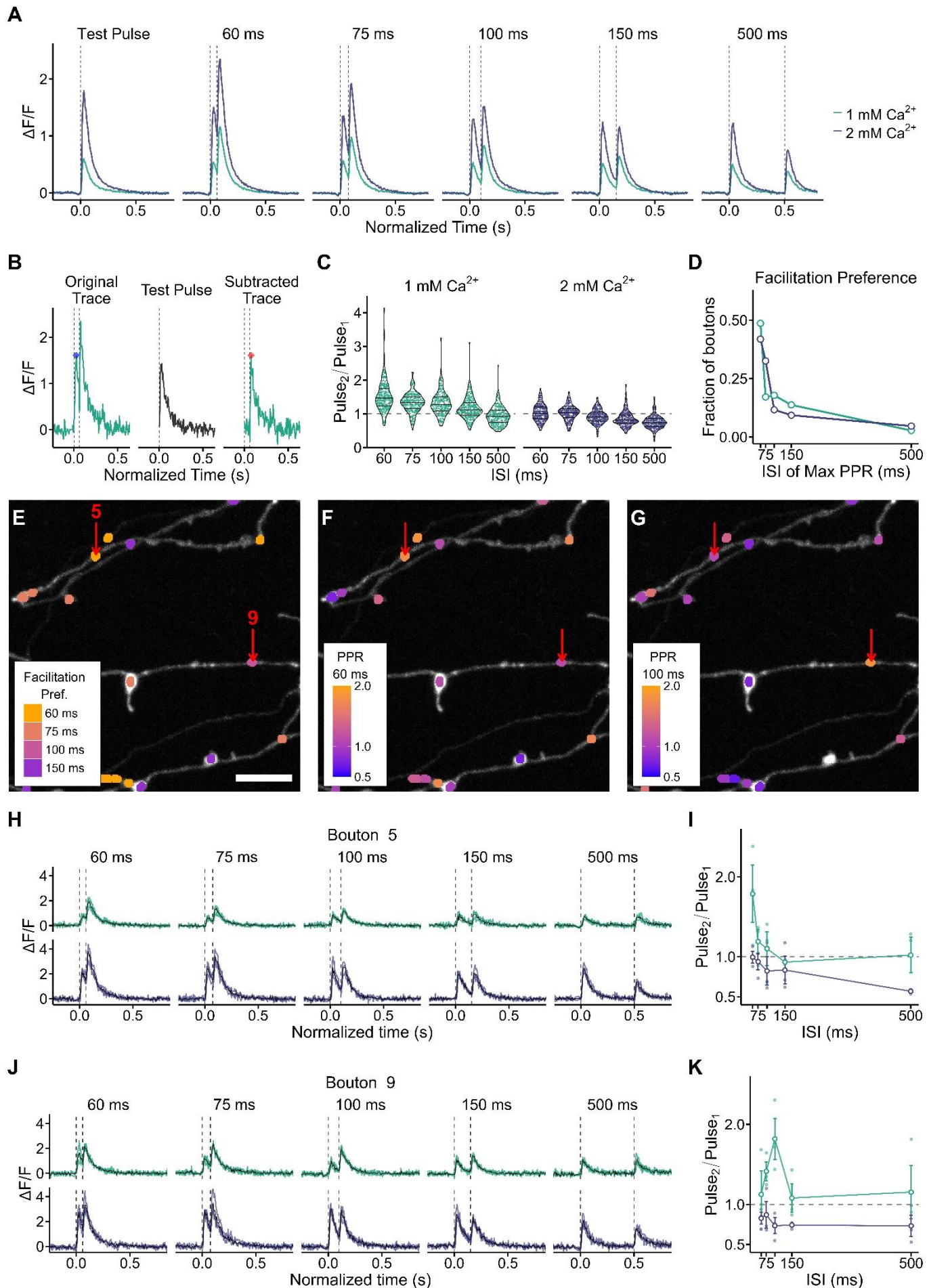
**Figure 5. iGluSnFR3 responses evoked by paired stimuli reveal heterogeneous short-term plasticity dynamics along the axonal arbor. A)** The averaged iGluSnFR3 response for each stimulus protocol administered in this experiment across $[Ca^{2+}]_{bath}$ = 1, 2 mM. Dashed vertical lines indicate the stimulus. **B)** Subtraction routine for determining paired-pulse ratios (PPRs) at individual boutons. *Left:* The amplitude of $Pulse_1$ (blue diamond) was the maximum $\Delta F/F$ observed within the first stimulus epoch in the unmodified, Original Trace for each trial. *Middle:* For each bouton, we determined the average iGluSnFR3 response to a single stimulus (Test Pulse) from three trials. *Right:* The amplitude of $Pulse_2$ (red diamond) was the maximum $\Delta F/F$ observed within the second stimulus epoch after subtracting the Test Pulse from the Original Trace for each trial. **C)** Violin plots showing the value of PPR as a function of $[Ca^{2+}]_{bath}$, interstimulus interval (ISI). Each colored dot indicates the mean value of PPR for each bouton. The dashed line indicates PPR = 1, the threshold between facilitation (PPR > 1) and depression (PPR < 1). Boutons largely depressed at all ISIs at $[Ca^{2+}]_{bath}$ = 2 mM. **D)** We categorized boutons according to which ISI produced the maximum value of PPR for boutons, the "Facilitation Bias". Of the facilitating boutons (PPR ≥ 1.1), 48.6% facilitated most strongly at ISI = 60 ms and $[Ca^{2+}]_{bath}$ = 1 mM. **E)** Facilitation bias mapped to an exemplar axonal arbor for $[Ca^{2+}]_{bath}$ = 1 mM. In this imaging region, no boutons facilitated most strongly at ISI = 500 ms. Scale bar = 5 μm. **F,G)** PPR mapped to the same axonal arbor as in **E**. Warmer colors indicate facilitation, while cooler colors indicate depression. **F)** PPRs for ISI = 60 ms, $[Ca^{2+}]_{bath}$ = 1 mM. **G)** PPRs for ISI = 100 ms, $[Ca^{2+}]_{bath}$ = 1 mM. In **E,F,G**, red arrows indicate boutons targeted for functional analysis. **H, I)** Bouton report for Bouton #5. **H)** The individual trial responses are color-coded by $[Ca^{2+}]_{bath}$ with the averaged response in black. **I)** PPR curves across ISIs for 1 and 2 mM $Ca^{2+}$ for Bouton #5. **J,K)** Bouton report for Bouton #9 as in **H,I**.

877

878

879

880

881

882

883

884

885

886

887

888

889

890

891
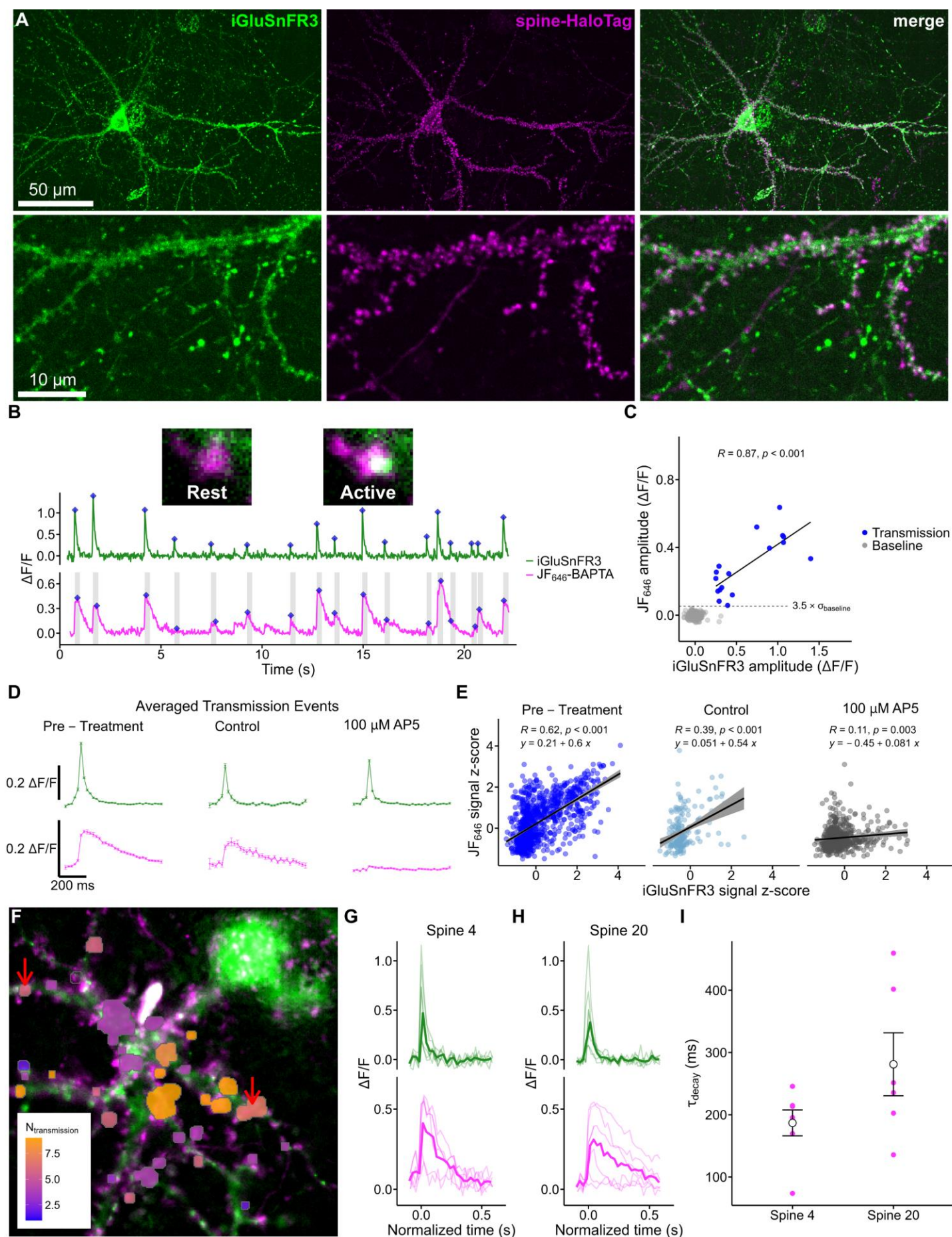
**Figure 6. Directly imaging NMDAR activation by spontaneous glutamate release at single dendritic spines using a dual fluorescent reporter approach. A)** An exemplar imaging region with a neuron expressing both iGluSnFR3 and spine-HaloTag dyed with $JF_{646}$-BAPTA-HTL-AM. spine-HaloTag accumulates in actin-rich compartments of the cell, like the dendritic spine head. Insets show a zoom-in of a stretch of dendrite. **B)** $\Delta F/F$ vs. time trace with spontaneous activity collected from iGluSnFR3 (green) and $JF_{646}$-BAPTA-AM (magenta) from a single dendritic spine head. In the green trace, our peak finding algorithm identified iGluSnFR3 signals and their peak maxima (blue diamonds). In the magenta trace, grey shaded regions in the magenta trace indicate regions around iGluSnFR3 signals. To identify the peaks of $JF_{646}$-BAPTA signals, we searched for local maxima in these grey shaded regions (blue diamonds). Insets show the corresponding dendritic spine at rest and during synaptic transmission. **C)** Scatterplot of $JF_{646}$ peak amplitude vs. the iGluSnFR3 peak amplitude for the spine in **B**. Our peak finding algorithm identified putative baseline indices as part of its baseline adjustment routine. For each dendritic spine, we calculated the standard deviation ($\sigma$) of the baseline noise. We set a threshold of $3.5\sigma$, and $JF_{646}$-BAPTA signals above this threshold were considered putative synaptic transmission events (blue dots). **D)** We collected all transmission events from spines before and after exposure to a control solution or a solution containing 100 µM AP5. The averaged waveforms show that AP5 treatment abolished $JF_{646}$-BAPTA signals, but not iGluSnFR3 signals, indicating that $JF_{646}$-BAPTA signals represent NMDAR-mediated $Ca^{2+}$ flux. **E)** We normalized transmission events by spine (z-score) and plotted the population correlations between iGluSnFR3 and $JF_{646}$-BAPTA signals. The strong positive correlation in the Pre-Treatment condition suggests that the amount of $Ca^{2+}$ fluxed by NMDARs is dependent on the local concentration of glutamate during NMDAR activation. The slope of the correlation is largely intact following treatment of spines with a control solution, while treatment with 100 µM AP5 abolished the correlation. The Pearson correlation coefficient (R) and statistical significance are indicated on each subplot. **F)** An exemplar imaging region with dendritic spine ROIs color-coded according to the recorded number of transmission events ($N_{transmission}$). Two spines are selected for comparative analysis, indicated by the red arrows. Scale bar = 10 µm. **G, H)** The time-aligned iGluSnFR3 and $JF_{646}$-BAPTA signals for each transmission event for Spine 4 and Spine 20. Average waveform is indicated by the bolded curve. **I)** Distribution of $\tau_{decay}$ vs. spine identity. $JF_{646}$-BAPTA signals at Spine 4 and Spine 20 possess distinct decay kinetics.
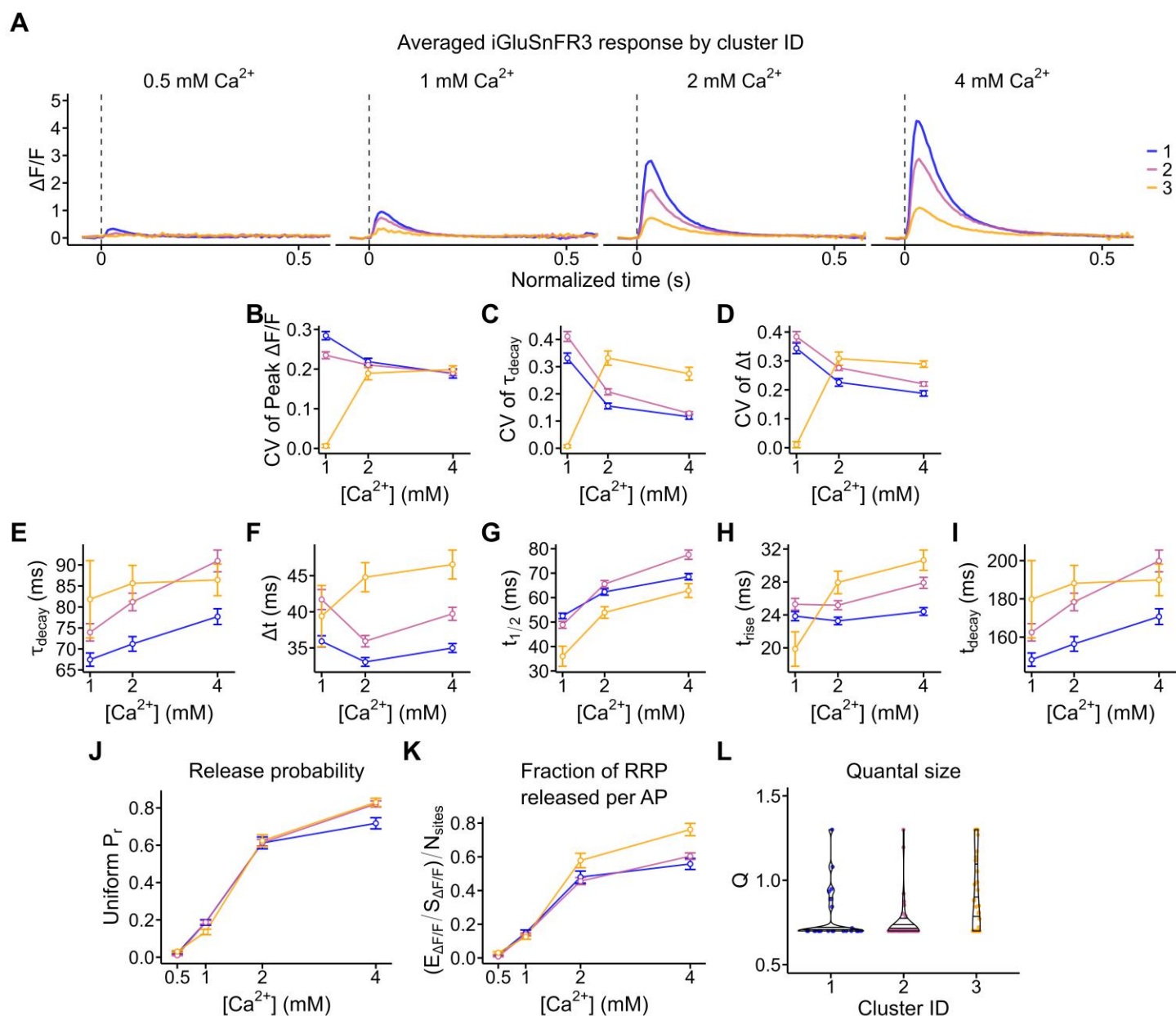
**Extended Data Figure 4. Additional functional properties of the three bouton classes suggest differences in the SV release machinery. A)** The average iGluSnFR3 response in response to stimulus across $[Ca^{2+}]_{bath}$ and cluster ID. For the plots presented in **B-G**, 0.5 mM $Ca^{2+}$ has been omitted due to the sparse data in cluster 2 and 3. **B)** Coefficient of variation (CV) of peak ΔF/F vs. $[Ca^{2+}]_{bath}$. **C)** CV of $\tau_{decay}$ vs. $[Ca^{2+}]_{bath}$. **D)** CV of Δt vs. $[Ca^{2+}]_{bath}$. **E)** $\tau_{decay}$ vs. $[Ca^{2+}]_{bath}$. **F)** Δt vs. $[Ca^{2+}]_{bath}$. **G)** $t_{1/2}$ vs. $[Ca^{2+}]_{bath}$. **H)** $t_{rise}$ (10-90%) vs. $[Ca^{2+}]_{bath}$. **I)** $t_{decay}$ (90-10%) vs. $[Ca^{2+}]_{bath}$. **J)** Uniform release probability, $P_r$ vs. $[Ca^{2+}]_{bath}$. **K)** RRP fraction released per AP ($E_{\Delta F/F}/S_{\Delta F/F}$)/$N_{sites}$ vs. $[Ca^{2+}]_{bath}$. **L)** Binomial model Q vs. cluster ID.

947
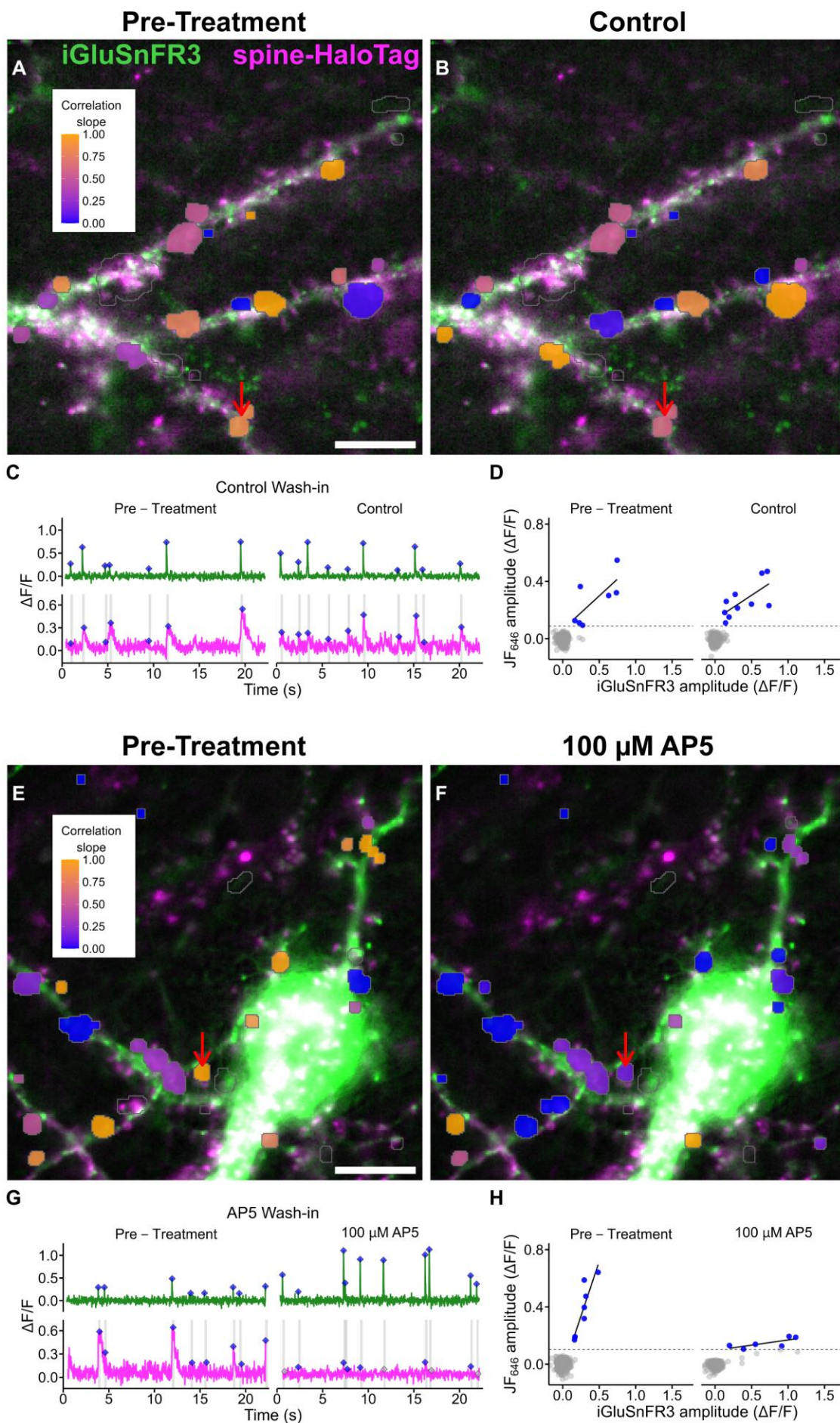
**Extended Data Figure 6. JF$_{646}$ signals correspond to NMDA receptor activation, as washing in 100 µM AP5 abolishes the correlation between iGluSnFR3 and Ca$^{2+}$ signals at dendritic spines.** **A,B)** An exemplar imaging region, scale bar = 10 µm. Spines that were active in the iGluSnFR3 channel were segmented and analyzed. Segmented spines are color-coded according to the slope of their correlation between JF$_{646}$ and iGluSnFR3 signals. The plots in **A, B**, show the same imaging region before (**A**) and after (**B**) wash-in of a control solution. **C, D**) Report on the activity at the spine indicated by the red arrow in **A**, **B**. **C)** The correlated iGluSnFR3 and JF$_{646}$ activity before and after wash-in of control solution. **D)** A scatter plot of JF$_{646}$ amplitude vs. iGluSnFR3 amplitude, before and after wash-in of control solution. Grey points indicate the amplitude correlation of putative baseline points. Blue points are transmission events. Dashed line indicates the +3.5σ threshold (where σ is the standard deviation of the baseline) above which an event could be considered synaptic transmission. The linear trend (black) shows the correlation between JF$_{646}$ signal amplitude and iGluSnFR3 signal amplitude. The slope of this line is the "correlation slope" shown in the color-coded plots of **A, B**. **E,F)** An exemplar imaging region, scale bar = 10 µm. The plots in **E, F**, show the same imaging region before (**E**) and after (**F**) wash-in of a solution containing 100 µM DL-AP5, an NMDAR antagonist. AP5 treatment reduced the correlation slope (cooler colors) for segmented spines as JF$_{646}$ signals were mostly abolished. This suggests that JF$_{646}$ signals correspond to NMDA receptor activation. **G, H)** Report on the activity at a spine indicated by the red arrow in **E**, **F**. **G)** The correlated iGluSnFR3 and JF$_{646}$ activity before and after wash-in of 100 µM DL-AP5. JF$_{646}$, but not iGluSnFR3 signals, were abolished following AP5 treatment. **H**) A scatter plot of JF$_{646}$ amplitude vs. iGluSnFR3 amplitude, before and after wash-in of 100 µM DL-AP5. The slope of the correlation decreases substantially following AP5 treatment.
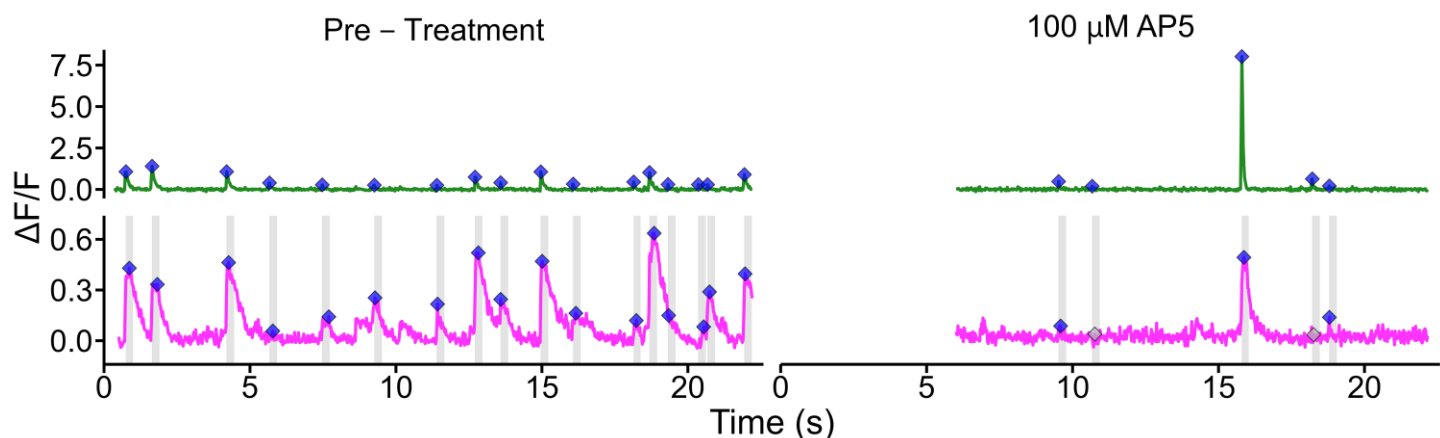
**Figure S1. Large iGluSnFR3 transients give rise to JF$_{646}$ signals even after treatment with 100 µM AP5.** Correlated iGluSnFR3 (green) and JF$_{646}$ (magenta) activity before and after wash-in of 100 µM AP5. Note that this is the same spine as displayed in main-text **Figure 6B**. The y-axis of the iGluSnFR3 plot has been rescaled to accommodate the extremely large spontaneous iGluSnFR3 transient observed after 100 µM AP5 treatment. The data suggest that when the glutamate concentration in the cleft is sufficiently large, it can briefly out-compete AP5 to activate NMDARs.
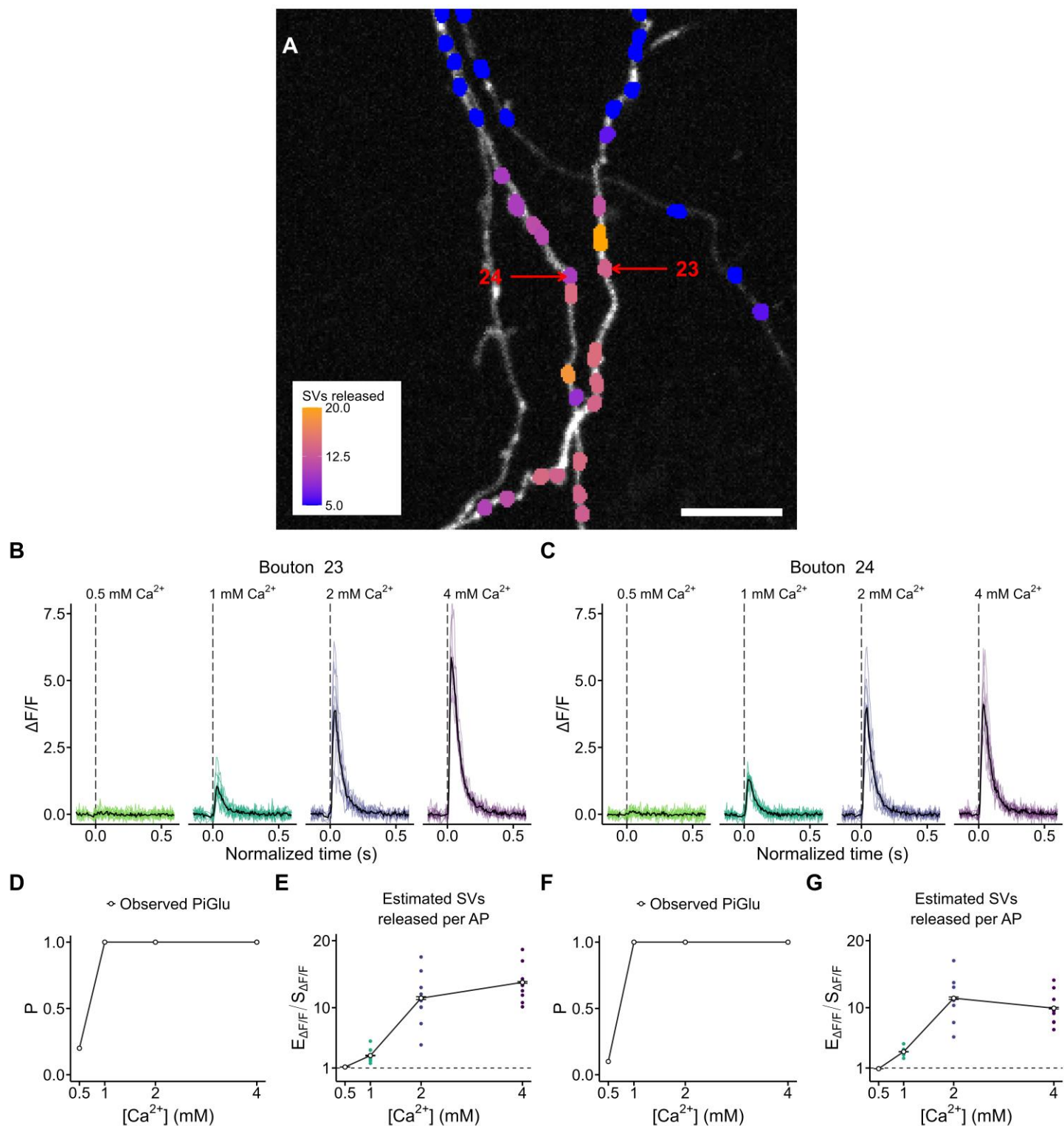
**Figure S2. Boutons separated by ~1.8 μm exhibit divergent iGluSnFR3 behavior. A)** The imaging region from **Figure 4I**, color-coded according to number of SVs released at 4 mM $Ca^{2+}$. Boutons 23 and 24 are indicated for further analysis. **B, C)** The iGluSnFR3 responses at all $[Ca^{2+}]_{bath}$ tested. Though the boutons are only separated by 1.8 μm on separate branches of the same axon, they exhibit divergent iGluSnFR3 behavior. **D,F)** $P_{iGlu}$ vs. $[Ca^{2+}]_{bath}$. **E,G)** Estimated SVs released per AP ($E_{\Delta F/F}/S_{\Delta F/F}$) vs. $[Ca^{2+}]_{bath}$. Note that Bouton 24 appears to exhaust at 4 mM $Ca^{2+}$.

# References

1. Südhof, TC & Malenka, RC. "Understanding Synapses: Past, Present, and Future." *Neuron*, **2018**, *60*, 469–476.

2. Abbott, LF, & Regehr, WG. "Synaptic computation." *Nature*, **2004**, *431*, 796–803.

3. Branco, T, & Staras, K. "The probability of neurotransmitter release: Variability and feedback control at single synapses." *Nature Reviews Neuroscience*, **2009**, *10*, 373–383.

4. Regehr, WG. "Short-term presynaptic plasticity." *Cold Spring Harbor Perspectives in Biology*, **2012**, *4*, 1–19.

5. O'Rourke, NA, Weiler, NC, Micheva, KD, & Smith, SJ. "Deep molecular diversity of mammalian synapses: Why it matters and how to measure it." *Nature Reviews Neuroscience*, **2012**, *13*, 365–379.

6. Grant, SGN, & Fransén, E. "The Synapse Diversity Dilemma: Molecular Heterogeneity Confounds Studies of Synapse Function." *Front. Synaptic Neurosci.*, **2020**, *12,* 1–8.

7. Xu, H, Oses-Prieto, JA, Khvotchev, M, Jain, S, Liang, J, Burlingame, A, & Edwards, RH. "Adaptor protein AP-3 produces synaptic vesicles that release at high frequency by recruiting phospholipid flippase ATP8A1." *Nature Neuroscience*, **2023**, *26*, 1685-1700.

8. Jackman, SL, Turecek, J, Belinsky, JE, & Regehr, WG. "The calcium sensor synaptotagmin 7 is required for synaptic facilitation." *Nature*, **2016**, *529*, 88–91.

9. Paoletti, P, Bellone, C, & Zhou, Q. "NMDA receptor subunit diversity : impact on receptor properties, synaptic plasticity and disease." *Nature Reviews Neuroscience*, **2013**, *14*, 383–400.

10. Carter, AG, & Sabatini, BL. "State-dependent calcium signaling in dendritic spines of striatal medium spiny neurons." *Neuron*, **2004**, *44*, 483–493.

11. Lin, MZ, & Schnitzer, MJ. "Genetically encoded indicators of neuronal activity." *Nature Neuroscience*, **2016**, *19*, 1142–1153.

12. Hao, Y, & Plested, AJR. "Seeing glutamate at central synapses." *Journal of Neuroscience Methods*, **2022**, *375*, 1–13.

13. Balaji, J, & Ryan, TA. "Single-vesicle imaging reveals that synaptic vesicle exocytosis and endocytosis are coupled by a single stochastic mode." *PNAS*, **2007**, *104*, 20576–20581.

14. Sakamoto, H, Ariyoshi, T, Kimpara, N, Sugao, K, Taiko, I, Takikawa, K, Asanuma, D, Namiki, S, & Hirose, K. "Synaptic weight set by Munc13-1 supramolecular assemblies." *Nature Neuroscience*, **2018**, *21*, 41–55.

15. Kleinfeld, D, Giovannucci, A, Friedrich, J, et al. "CaImAn an open source tool for scalable calcium imaging data analysis." *eLife*, *8*, **2019**, 1–45.

16. Cai, C, Dong, C, Friedrich, J, Rozsa, M, Pnevmatikakis, EA, & Giovannucci, A. "FIOLA: an accelerated pipeline for fluorescence imaging online analysis." *Nature Methods*, **2023**, *20*, 1417–1425.

17. Cai, C, Friedrich, J, Singh, A, Eybposh, MH, Pnevmatikakis, EA, Podgorski, K, & Giovannucci, A. "VolPy: Automated and scalable analysis pipelines for voltage imaging datasets." *PLoS Computational Biology*, **2021**, *17*, 1–27.

18. Aggarwal, A, et al. "Glutamate indicators with improved activation kinetics and localization for imaging synaptic transmission." *Nature Methods*, **2023**, *20,* 925-934.

19. Dürst, CD, Wiegert, JS, Schulze, C. *et al.* "Vesicular release probability sets the strength of individual Schaffer collateral synapses." *Nat Commun* **2022**, *13*, 6126.

20. Helassa, N, Dürst, CD, Coates, C, Kerruth, S, Arif, U, Schulze, C, Simon Wiegert, J, Geeves, M, Oertner, TG, & Török, K. "Ultrafast glutamate sensors resolve high-frequency release at Schaffer collateral synapses." *PNAS*, **2018**, *115*, 5594–5599.

21. Courtney, NA, Briguglio, JS, Bradberry, MM, Greer, C, & Chapman, ER. "Excitatory and Inhibitory Neurons Utilize Different Ca2+ Sensors and Sources to Regulate Spontaneous Release." *Neuron*, **2018**, *98*, 977-991.

22. Wang, Y, Wang, C, Ranefall, P, Broussard, GJ, Wang, Y, Shi, G, Lyu, B, Wu, CT, Wang, Y, Tian, L, & Yu, G. "SynQuant: An automatic tool to quantify synapses from microscopy images." *Bioinformatics*, **2020**, *36*, 1599–1606.

23. Mendonça, PRF, Tagliatti, E, Langley, H, Kotzadimitriou, D, Zamora-Chimal, CG, Timofeeva, Y, & Volynski, KE. "Aynchronous glutamate release is enhanced in low release efficacy synapses and dispersed across the active zone." *Nature Communications*, **2022**, *13*, 1–17.

24. Taschenberger, H, Woehler, A, & Neher, E. "Superpriming of synaptic vesicles as a common basis for intersynapse variability and modulation of synaptic strength." *PNAS*, **2016**, *113*, E4548–E4557.

25. Maschi, D, & Klyachko, VA. "Spatiotemporal dynamics of multi-vesicular release is determined by heterogeneity of release sites within central synapses." *eLife*, **2020**, *9*, 1–20.

26. Tang, AH, Chen, H, Li, TP, Metzbower, SR, MacGillavry, HD, & Blanpied, TA. "A trans-synaptic nanocolumn aligns neurotransmitter release to receptors." *Nature*, **2016**, *536*, 210–214.

27. Kaeser, PS, & Regehr, WG. "The readily releasable pool of synaptic vesicles." *Current Opinion in Neurobiology*, **2017**, *43*, 63–70.

28. Clements, JD, & Silver, RA. "Unveiling synaptic plasticity : a new graphical and analytical approach." *Trends in Neurosciences*, **2000**, *23*, 105–113.

29. Malagon, G, Miki, T, Llano, I, Neher, E, & Marty, A. "Counting vesicular release events reveals binomial release statistics at single glutamatergic synapses." *Journal of Neuroscience*, **2016**, *36*, 4010–4025.

30. Glasgow, SD, McPhedrain, R, Madranges, JF, Kennedy, TE, & Ruthazer, ES. "Approaches and limitations in the investigation of synaptic transmission and plasticity." *Frontiers in Synaptic Neuroscience*, **2019**, *11*, 1–16.

31. Sakamoto, H, Ariyoshi, T, Kimpara, N, Sugao, K, Taiko, I, Takikawa, K, Asanuma, D, Namiki, S, & Hirose, K. "Synaptic weight set by Munc13-1 supramolecular assemblies." *Nature Neuroscience*, **2018**, *21*, 41–55.

32. Kusick, GF, Chin, M, Raychaudhuri, S, Lippmann, K, Adula, KP, Hujber, EJ, Vu, T, Davis, MW, Jorgensen, EM, & Watanabe, S. "Synaptic vesicles transiently dock to refill release sites." *Nature Neuroscience*, **2020**, *23*, 1329–1338.

33. McInnes, L, Healy, J, Saul, N & Großberger, L. "UMAP: uniform manifold approximation and projection." *J. Open Source Softw.* **2018**, *3*, 861.

34. Volk, L, Chiu, SL, Sharma, K, & Huganir, RL. "Glutamate Synapses in Human Cognitive Disorders." *Annual Review of Neuroscience*, **2015**, *38*, 127–149.

35. Fan, LZ, Nehme, R, Adam, Y, Jung, ES, Wu, H, Eggan, K, Arnold, DB, & Cohen, AE. "All-optical synaptic electrophysiology probes mechanism of ketamine-induced disinhibition." *Nature Methods*, **2018**, *15*, 823–831.

36. Dana, H, et al. "Sensitive red protein calcium indicators for imaging neural activity." *eLife*, **2016**, *5*, 1–24.

37. Los, GV, Encell, LP, Mcdougall, MG, Hartzell, DD, Karassina, N, Simpson, D, Mendez, J, Zimmerman, K, Otto, P, Vidugiris, G, Zhu, J, Darzins, A, Klaubert, DH, Bulleit, RF, & Wood, KV. "HaloTag: A Novel Protein Labeling Technology for Cell Imaging and Protein Analysis." *ACS Chemical Biology*, **2008**, *3*, 373–382.

38. Deo, C, Sheu, S, Seo, J, Clapham, DE, & Lavis, LD. "Isomeric Tuning Yields Bright and Targetable Red $Ca^{2+}$ Indicators." *JACS*, **2019**, *141*, 13734–13738.

39. Metzbower, SR, Joo, Y, Benavides, DR, & Blanpied, TA. "Properties of Individual Hippocampal Synapses Influencing NMDA-Receptor Activation by Spontaneous Neurotransmission." *eNeuro*, **2019**, *6*, 1–17.

40. Lester, RAJ, Clements, JD, Westbrook, GL, & Jahr, CE. "Channel kinetics determine the time course of NMDA receptor-mediated synaptic currents." *Nature*, **1990**, *346*, 565–567.

41. Niswender, CM & Conn, PJ. "Metabotropic Glutamate Receptors: Physiology, Pharmacology, and Disease." *Annu Rev Pharmacol Toxicol*. **2010**, *50*, 295–322.

42. Chen, JJ, Kaufmann, WA, Chen, C, Arai, I, Kim, O, Shigemoto, R, & Jonas, P. "Developmental transformation of Ca2+ channel-vesicle nanotopography at a central GABAergic synapse." *Neuron*, **2024**, *112*, 755-771.

43. Barri, A, Wiechert, MT, Jazayeri, M, & DiGregorio, DA. "Synaptic basis of a sub-second representation of time in a neural circuit model." *Nature Communications*, **2022**, *13*, 1–18.

44. Bradberry, MM & Chapman, ER. "All-optical monitoring of excitation secretion coupling demonstrates that SV2A functions downstream of evoked Ca2+ entry." *J. Physiology*, **2022**, *600*, 645–654.

45. Almada, P, Pereira, PM, Culley, S, Caillol, G, Boroni-Rueda, F, Dix, CL, Charras, G, Baum, B, Laine, RF, Leterrier, C, & Henriques, R. "Automating multimodal microscopy with NanoJ-Fluidics." *Nature Communications*, **2019**, *10*, 1–9.

46. Dharmasri, PA, Levy, AD, & Blanpied, TA. "Differential nanoscale organization of excitatory synapses onto excitatory vs. inhibitory neurons." *PNAS*, **2024**, *121*, 1–11.

47. Padfield D, O'Sullivan H, Pawar S. "rTPC and nls.multstart: A new pipeline to fit thermal performance curves in *R*." *Methods Ecol Evol*. **2021**, *12*, 1138–1143.